A mechanical analysis of variable angle-tow composite plates through variable kinematics models based on Carrera's unified formulation

D.A. Iannotta, G. Giunta, Marco Montemurro

Composite Structures 327 (2024) 117717

Contents lists available at ScienceDirect

Composite Structures

journal homepage: www.elsevier.com/locate/compstruct

A mechanical analysis of variable angle-tow composite plates through variable kinematics models based on Carrera's unified formulation

D.A. Iannotta [a,b,c], G. Giunta [a,*], M. Montemurro [c]

[a] Luxembourg Institute of Science and Technology, L-4362 Esch-sur-Alzette, 5 avenue des Hauts-Fourneaux, Luxembourg
[b] University of Luxembourg, L-4365 Esch-sur-Alzette, 2 avenue de l'Université, Luxembourg
[c] Arts et Métiers Institute of Technology, Université de Bordeaux, CNRS, INRA, Bordeaux INP, HESAM Université, I2M UMR 5295, F-33405 Talence, France

ARTICLE INFO

Keywords:
Static analysis
Finite element method
Variable angle-tows plates
Carrera's unified formulation
Reissner's mixed variational theorem

ABSTRACT

Variable Angle-Tow (VAT) laminates offer a promising alternative to straight fiber composites. By varying fibers orientation within the structure plane, ambitious design and performance goals can be achieved. However, the wider design space results in a more complex problem with more parameters to consider. Carrera's Unified Formulation (CUF) has been used in previous works performing buckling, vibrational and stress analyses of VAT plates. Usually, one-dimensional (1D) CUF beam models are used, while two-dimensional (2D) plate models are obtained as a particular case of shells by considering a null curvature. In most cases, a linear law is considered to describe the variation of fibers orientation in the main plane of the structure. The purpose of this article is to extend the CUF 2D plate finite elements family to the mechanical analysis of composite laminated plate structures with curvilinear fibers. The main contribute consists in the development of a CUF FE model within the Reissner's Mixed Variational Theorem (RMVT) context for an improved calculation of the out-of-plane stress components. Results show that RMVT can predict in-plane stresses and satisfy the though-the-thickness transverse stresses continuity due to inter-layer equilibrium. The accuracy of RMVT-based models is also investigated using two different approximation points distributions along the plates thickness.

1. Introduction

In the last decades, composite materials have shown attractive properties for aerospace applications. This is due to the high stiffness-to-weight ratio they exhibit, which is useful in those contexts where both weight and mechanical performance of the system are considered as primary properties [1]. Straight fibers composites with constant thickness are typically used, but a common thought is that the potential of fiber reinforced structures has not been fully exploited yet. For example, it is not possible to fully profit from the directional properties of this kind of materials by keeping the fiber orientation constant in each layer. This limitation could be particularly restrictive for geometries which present geometrical discontinuities like holes. Modern production techniques, like additive manufacture processes, allow to overcome these limitations, going beyond the classical design configurations of composites. Variable-Stiffness Composite (VSC) structures can be obtained with different approaches [2], involving the point-wise variation of thickness and material properties. For aerospace applications, the idea of locally varying fibers angle along the structures in-plane directions appears to be one of the most promising to improve the versatility of composite materials. In this way, VAT laminates can be obtained allowing to expand the design space of a specific structure. One of the principal drawbacks of using VATs is related to the complexity of the analysis. In these cases, it is necessary to consider an increased number of unknowns and unfeasible fibers patterns could be obtained in an optimization process.

In the following, a short review of common methods that are used for the analysis of VSCs mechanical response is presented, with a major focus on VAT cases. One of the first methods that has been developed assumes that the fibers angle is constant within each element in a Finite Element Method (FEM) solution. In this manner, the continuous variation of fibers direction is approximated in a stepwise discrete way. This is, for instance, the case presented by Hyer and Charette [3], where, in each element, the fibers are aligned along the principal stress direction to improve the tensile strength of a plate. A similar approach was applied by Hyer and Lee in [4], where a sensitivity analysis was used to improve the buckling load of a composite plate. In order to maximize the buckling load of the entire structure, the orientation associated with the maximum buckling load was determined for each element through multiple analyses. Finally, the sensitivity of the buckling load to small changes in the orientation of each element was

* Corresponding author.
E-mail address: gaetano.giunta@list.lu (G. Giunta).

https://doi.org/10.1016/j.compstruct.2023.117717
Received 12 July 2023; Received in revised form 11 September 2023; Accepted 7 November 2023
Available online 10 November 2023

analyzed using a gradient-search technique. The technique involved iteratively adjusting the orientations of the elements to optimize the overall buckling load while considering the influence of element interaction. The main drawback of these approaches lies in the use of an element-wise representation of the fibers path. Without the use of an appropriate continuous and smooth representation or the fiber orientation angle, the optimized solutions may be characterized by a discontinuous fibers path, thus cannot be manufactured and require a time-consuming post-processing phase to correct [5]. This often results in a mismatch between the structural responses calculated on the optimized fibers path and those calculated after post-processing (recovery) of the optimized solution.

In [6], the classical lamination theory was used to obtain the equilibrium equations of VAT plates. The obtained governing equations were solved both in closed-form and through an iterative numerical technique to study plates under uniaxial compression. The same theory was used by Gürdal et al. in [7], where the Rayleigh–Ritz method was used in buckling analyses of VAT plates. Non-linear static analyses of VAT shells were performed by Gupta and Pradyumna [8], where the Third-order Shear Deformation Theory (TSDT) was coupled with the Murakami zigzag function: von Kármán relations were used in order to develop a non-linear problem solved through the Newton–Raphson method. Non-linear problems were also studied by Akhavan, Ribeiro, and De Moura [9] through the Newmark method with p-version finite elements based on TSDT. Günay and Timarci [10] studied the static behavior of single-cell VSC beams with closed cross-section by using two-node beam elements characterized by seven variables per each node. Static and dynamic analyses of VAT plates were performed by Sharma et al. [11], piezoelectric layers were also considered and eight-node isoparametric elements based on the first-order shear deformation theory were used. The effects of delamination and fibers angle variation were considered as well. The Hellinger–Reissner mixed variational principle was used by Groh and Weaver [12,13] to study tow-steered composite plates including zigzag effects. The same mixed approach was used by Trinh et al. [14] for the flexural analysis of VSC beams in the framework of an inverse differential quadrature method. Sciascia et al. [15] proposed an innovative approach for the dynamic analysis of prestressed VAT shells. The Ritz formulation was used for the eigenvalue analysis, considering the first-order shear deformation theory to describe the shell kinematics. Olivieri and Milazzo [16] analyzed the postbuckling behavior of VAT stiffened panels. The structures were modeled through the domain decomposition by enforcing the boundary conditions for each component. The Rayleigh–Ritz method was used to solve the problem governing equations obtained through the first-order shear deformation theory.

The introduction of VSCs complicates the optimization analysis since the material anisotropy affects multiple scales of the problem. Also manufacturing constraints play an important role and they should be considered during the analysis to obtain feasible (i.e., manufacturable) solutions. The Multi-Scale Two-Level (MS2L) approach allows to split the optimization problem in two sub-problems. During the first step, the composite is represented as an equivalent homogeneous anisotropic plate: the aim of this phase is to determine the best distribution of geometrical and mechanical design variables governing the behavior of the VSC structure at this scale. Among the different representations of the anisotropy at the macroscopic scale, the most efficient one is that based on polar parameters (see Montemurro [17,18]). During the second step, the goal is to find at least one stack matching the optimized distribution of the polar parameters resulting from the first optimization step. Montemurro and Catapano [19] applied the MS2L method to VAT plates to optimize their buckling response: B-spline surfaces allow to obtain a continuous and differentiable distribution of the polar parameters over the structure, while manufacturing constraints are introduced during the second step. A rigorous theoretical/numerical framework for the gradient-based optimization of VAT structure was introduced by Montemurro and Catapano in [20,21], where the formal expression of the gradient of the compliance was provided and the constraint related to the minimum admissible radius of curvature of the tow at the mesoscopic scale was formulated as an equivalent constraint in the space of the polar parameters at the macroscopic scale during the first step. Fiordilino, Izzi and Montemurro [22] generalized the framework by providing the analytical expression of the gradients of objective and constraint functions were derived for buckling problems. Finally, the failure index optimization was analyzed by Catapano and Montemurro [23], while failure load maximization and mass minimization were performed by Izzi, Catapano and Montemurro [24].

A method which allows to study bi-dimensional VAT structures by using an arbitrary expansion order along the thickness is represented by Carrera's Unified Formulation. This formulation can be used to obtain both Equivalent Single Layer (ESL) and Layer-Wise (LW) descriptions of plate kinematics in the context of a specific predefined variational statement (Carrera [25,26]). For example, Carrera, Giunta and Brischetto [27] used CUF to develop a Navier closed-form solution for the static analysis of isotropic plates under several loading conditions. The same approach was used by Carrera and Giunta [28] to perform failure analyses of isotropic plates. A further extension of this method was shown by Giunta et al. in [29], where the indentation failure analysis of composite sandwich plates was performed. Hui et al. [30] used a family of 1D CUF models in order to perform the multiscale nonlinear analysis of composite beam structures, through the asymptotic numerical method. The effect of microscopic imperfections on the macroscale response was investigated by considering sinusoidal geometries as fibers defects. CUF has also been applied to modern computing techniques like the data-driven approach. For example, Hui et al. [31] used 1D CUF models within the data-driven computational mechanics paradigm in order to perform the static analysis of beam structures. Results showed that the accuracy is influenced by the number of layers of the database. Viglietti et al. [32] and Fallahi et al. [33] used a 1D CUF model for free-vibration and buckling analyses of VATs. Buckling optimization of VATs was studied by Fallahi et al. [34] by applying a genetic algorithm to a 1D CUF model. Also shell models were studied for VAT cases to perform stress analyses [35]. Some defects related to the manufacturing process of VAT plates can be simulated with various stochastic techniques as shown by Pagani and Sánchez-Majano [36,37] and Sánchez-Majano et al. [38].

An extension of CUF allows using a different expansion for each component of the displacement vector. This generalization was applied for the first time to the study of VSC plates with a LW model by Demasi et al. [39], while it was extended also to ESL theories in [40] and plates with a central circular cut out in [41]. Santarpia and Demasi [42] used this approach for nonlinear analyses of VATs where large displacements and rotations were considered. In all cases, triangular elements were used to perform the analyses. Ritz's method was used within CUF by Vescovini and Dozio [43] for vibrational and buckling analyses. Static analyses of VATs were presented by Tornabene et al. [44], who used shell elements and the governing equations were solved through the generalized differential quadrature method.

A further advantage of CUF is represented by the possibility to combine it with different variational formulations. Reissner's Mixed Variational Theorem is an alternative to the classic Principle of Virtual Displacements, where both displacements and out-of-plane transverse stresses are considered as unknowns. RMVT was widely used within CUF for the study of straight fibers composite structures. For example, Carrera and Demasi [45] showed how to apply RMVT to CUF from a theoretical point of view, while in the second part of the article [46] static analyses were performed on straight fibers plates.

To the best of the authors knowledge, CUF has been applied to the study of VATs mainly considering PVD as functional. To this end, the aim of this work is to extend this framework to the RMVT formulation to develop a family of plate finite elements which will be able to better predict the out-of-plane stresses when curvilinear fibers are used. This

approach was used in a previous work by Giunta et al. [47] for the modal analysis of VAT plates.

The remainder of the paper is as follows. Section 2 introduces the CUF approach and shows its application to the two mentioned variational statements. In Section 3, three benchmark problems are considered. For each of them, linear static analyses are performed to discuss differences between PVD, RMVT and reference solutions obtained in Abaqus by using three-dimensional (3D) elements. Finally, Section 4 presents the concluding observations.

2. Carrera's unified formulation

A plate is a structure without curvature characterized by an out-of-plane dimension that is significantly smaller (i.e., negligible) than the minimum in-plane dimension. Typically, the out-of-plane dimension is the thickness h, defined along the z axis of the structure, while the in-plane dimensions are indicated as a and b which refer, respectively, to the characteristic lengths along x and y axes, respectively. The geometry and the global reference system of the problem are shown in Fig. 1. The displacement field is expressed as:

$$\mathbf{u} = \left\{ \begin{array}{c} u_x \\ u_y \\ u_z \end{array} \right\}. \tag{1}$$

The strain vector (Voigt's notation) can be divided in two parts representing the in-plane and out-of-plane components:

$$\boldsymbol{\epsilon}_p = \left\{ \begin{array}{c} \epsilon_{xx} \\ \epsilon_{yy} \\ \epsilon_{xy} \end{array} \right\}, \quad \boldsymbol{\epsilon}_n = \left\{ \begin{array}{c} \gamma_{xz} \\ \gamma_{yz} \\ \gamma_{zz} \end{array} \right\}. \tag{2}$$

The hypothesis of small displacements allows using a linear strains–displacements relation:

$$\begin{aligned} \boldsymbol{\epsilon}_p &= \mathbf{D}_p \mathbf{u} \,, \\ \boldsymbol{\epsilon}_n &= \left(\mathbf{D}_{n\Omega} + \mathbf{D}_{nz} \right) \mathbf{u} \,, \end{aligned} \tag{3}$$

where $\mathbf{D}_p, \mathbf{D}_{n\Omega}$ and $\mathbf{D}_{nz}$ are differential operators:

$$\begin{aligned} \mathbf{D}_p &= \left[\begin{array}{ccc} \frac{\partial}{\partial x} & 0 & 0 \\ 0 & \frac{\partial}{\partial y} & 0 \\ \frac{\partial}{\partial y} & \frac{\partial}{\partial x} & 0 \end{array} \right], \quad \mathbf{D}_{n\Omega} = \left[\begin{array}{ccc} 0 & 0 & \frac{\partial}{\partial x} \\ 0 & 0 & \frac{\partial}{\partial y} \\ 0 & 0 & 0 \end{array} \right], \\ \mathbf{D}_{nz} &= \left[\begin{array}{ccc} \frac{\partial}{\partial z} & 0 & 0 \\ 0 & \frac{\partial}{\partial z} & 0 \\ 0 & 0 & \frac{\partial}{\partial z} \end{array} \right]. \end{aligned} \tag{4}$$

The same consideration can be applied to stresses:

$$\boldsymbol{\sigma}_p = \left\{ \begin{array}{c} \sigma_{xx} \\ \sigma_{yy} \\ \sigma_{xy} \end{array} \right\}, \quad \boldsymbol{\sigma}_n = \left\{ \begin{array}{c} \sigma_{xz} \\ \sigma_{yz} \\ \sigma_{zz} \end{array} \right\}. \tag{5}$$

Hooke's law reads:

$$\begin{aligned} \boldsymbol{\sigma}_p &= \widetilde{\mathbf{C}}_{pp} \boldsymbol{\epsilon}_p + \widetilde{\mathbf{C}}_{pn} \boldsymbol{\epsilon}_n \,, \\ \boldsymbol{\sigma}_n &= \widetilde{\mathbf{C}}_{np} \boldsymbol{\epsilon}_p + \widetilde{\mathbf{C}}_{nn} \boldsymbol{\epsilon}_n \,, \end{aligned} \tag{6}$$

where the terms $\widetilde{\mathbf{C}}_{pp}, \widetilde{\mathbf{C}}_{pn}, \widetilde{\mathbf{C}}_{np}$ and $\widetilde{\mathbf{C}}_{nn}$ are the components of the material stiffness matrix.

2.1. Variable angle-tow composite plates

When considering VAT structures, the components of the material stiffness matrix vary along the in-plane directions. It is possible to write the equation which allows to rotate the material stiffness matrix $\mathbf{C}$ according to a specific angle θ around the z-axis as:

$$\widetilde{\mathbf{C}} = \mathbf{T}\mathbf{C}\mathbf{T}^T \,, \tag{7}$$

where $\mathbf{C}$ is the material stiffness matrix in the material reference system, while $\widetilde{\mathbf{C}}$ is the same matrix after a rotation. Matrix $\mathbf{T}$ represents the rotation matrix which depends on the angle θ. For the sake of brevity, the components of $\mathbf{C}$ and $\mathbf{T}$ are not reported here. They can be found in Reddy [48]. A linear variation law can be expressed as:

$$\theta(\alpha) = \Phi + T_0 + \frac{T_1 - T_0}{d} |\alpha| \,. \tag{8}$$

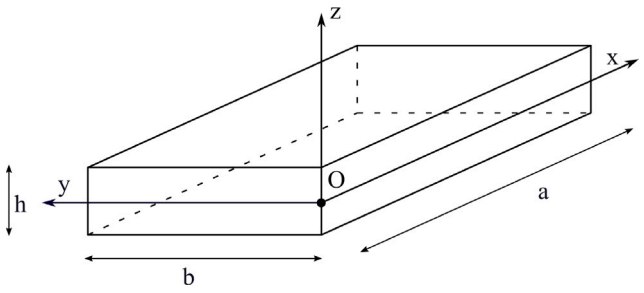

Fig. 1. Plate geometry and reference system.

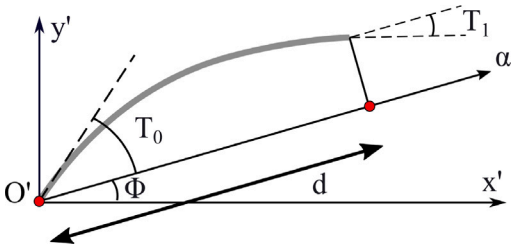

Fig. 2. Example of in-plane fibers path.

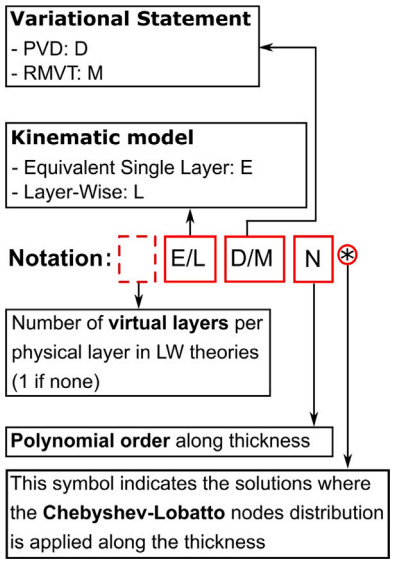

Fig. 3. Acronym system.

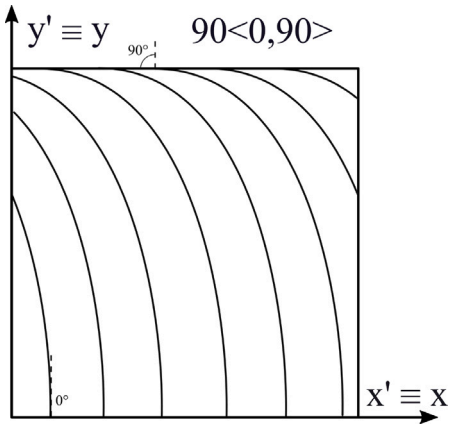

Fig. 4. In-plane fibers variation path, case 1.

The angle Φ describes the original direction along which θ varies, α is a generic spatial variable obtained as $\alpha = x' \cos(\Phi) + y' \sin(\Phi)$. x' and y' denote the axes of the angle reference system. T_0 is the starting angle of the fiber when $\alpha = 0$, while T_1 is the angle of the fiber when $\alpha = d$. Fig. 2 represents an example of fibers path. As shown in Fig. 2, fibers angle is always measured with respect to x' axis for all the analysis cases. The variation direction of θ can be x', y' or a combination of the two, for this reason it is specified case by case. In this work, the following notation (based upon the above introduced parameters) is used in order to describe the in-plane fibers path: $\Phi < T_0, T_1 >$. Further details about fibers variation law can be found in Gürdal et al. [7].

2.2. Variational formulation

PVD and RMVT variational statements are considered in order to obtain the problem governing equations. The main difference is that the PVD considers only displacements as unknowns, whereas the RMVT includes also the transverse stresses $\boldsymbol{\sigma}_n$ among the unknowns. For the PVD case, the following equation applies:

$$\int_\Omega \int_h \left(\delta\boldsymbol{\epsilon}_{pG}^T \, \boldsymbol{\sigma}_{pH} + \delta\boldsymbol{\epsilon}_{nG}^T \, \boldsymbol{\sigma}_{nH} \right) \, dz \, d\Omega = \delta L_e \,, \tag{9}$$

where the subscript 'G' refers to the components obtained from geometrical relations in Eq. (3), subscript 'H' refers to the components obtained from Hooke's law in Eq. (6) and subscript 'T' refers to the transpose of a vector/matrix. Ω is the in-plane middle surface of the plate, L_e is the work of the external forces and delta stands for a virtual variation. For the RMVT case, the variational statement is:

$$\int_\Omega \int_h \left[\delta\boldsymbol{\epsilon}_{pG}^T \, \boldsymbol{\sigma}_{pH} + \delta\boldsymbol{\epsilon}_{nG}^T \, \boldsymbol{\sigma}_{nM} + \delta\boldsymbol{\sigma}_{nM}^T \left(\boldsymbol{\epsilon}_{nG} - \boldsymbol{\epsilon}_{nH} \right) \right] \, dz \, d\Omega = \delta L_e \,, \tag{10}$$

where the 'M' subscript refers to the transverse stress components considered as unknowns in the mixed formulation. In the RMVT formulation, Hooke's law is expressed as follows:

$$\begin{aligned} \boldsymbol{\sigma}_{pH} &= \hat{\mathbf{C}}_{pp} \boldsymbol{\epsilon}_{pG} + \hat{\mathbf{C}}_{pn} \boldsymbol{\sigma}_{nM} \,, \\ \boldsymbol{\epsilon}_{nH} &= \hat{\mathbf{C}}_{np} \boldsymbol{\epsilon}_{pG} + \hat{\mathbf{C}}_{nn} \boldsymbol{\sigma}_{nM} \,, \end{aligned} \tag{11}$$

where $\hat{\mathbf{C}}_{pp}$, $\hat{\mathbf{C}}_{pn}$, $\hat{\mathbf{C}}_{np}$ and $\hat{\mathbf{C}}_{nn}$ are obtained by the following transformation (see Carrera and Demasi [45]):

$$\begin{aligned} \hat{\mathbf{C}}_{pp} &= \widetilde{\mathbf{C}}_{pp} - \widetilde{\mathbf{C}}_{pn} \widetilde{\mathbf{C}}_{nn}^{-1} \widetilde{\mathbf{C}}_{np} \,, \\ \hat{\mathbf{C}}_{pn} &= \widetilde{\mathbf{C}}_{pn} \widetilde{\mathbf{C}}_{nn}^{-1} \,, \\ \hat{\mathbf{C}}_{np} &= -\widetilde{\mathbf{C}}_{nn}^{-1} \widetilde{\mathbf{C}}_{np} \,, \\ \hat{\mathbf{C}}_{nn} &= \widetilde{\mathbf{C}}_{nn}^{-1} . \end{aligned} \tag{12}$$

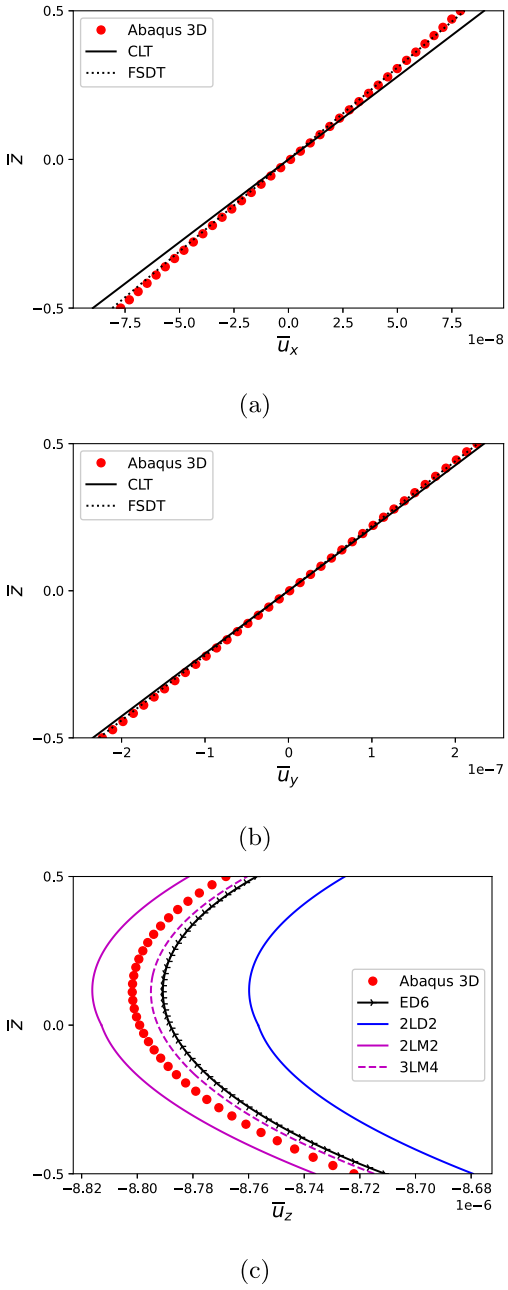

Fig. 5. Dimensionless displacements at $(a/2, b/2)$ versus the dimensionless thickness, case 1, $a/h = 10$.

Regarding the work of external loads, for example, in case of a pressure load applied to the plate middle surface, the term δL_e can be expressed as:

$$\delta L_e = \int_\Omega \delta \mathbf{u}^T \, \mathbf{p} \, d\Omega \,, \tag{13}$$

where $\mathbf{p}$ is a surface load.

2.3. Kinematic assumption and finite element approximation

In order to express the primary unknowns, CUF uses an axiomatic approach along the through-the-thickness direction (see Carrera [26]).

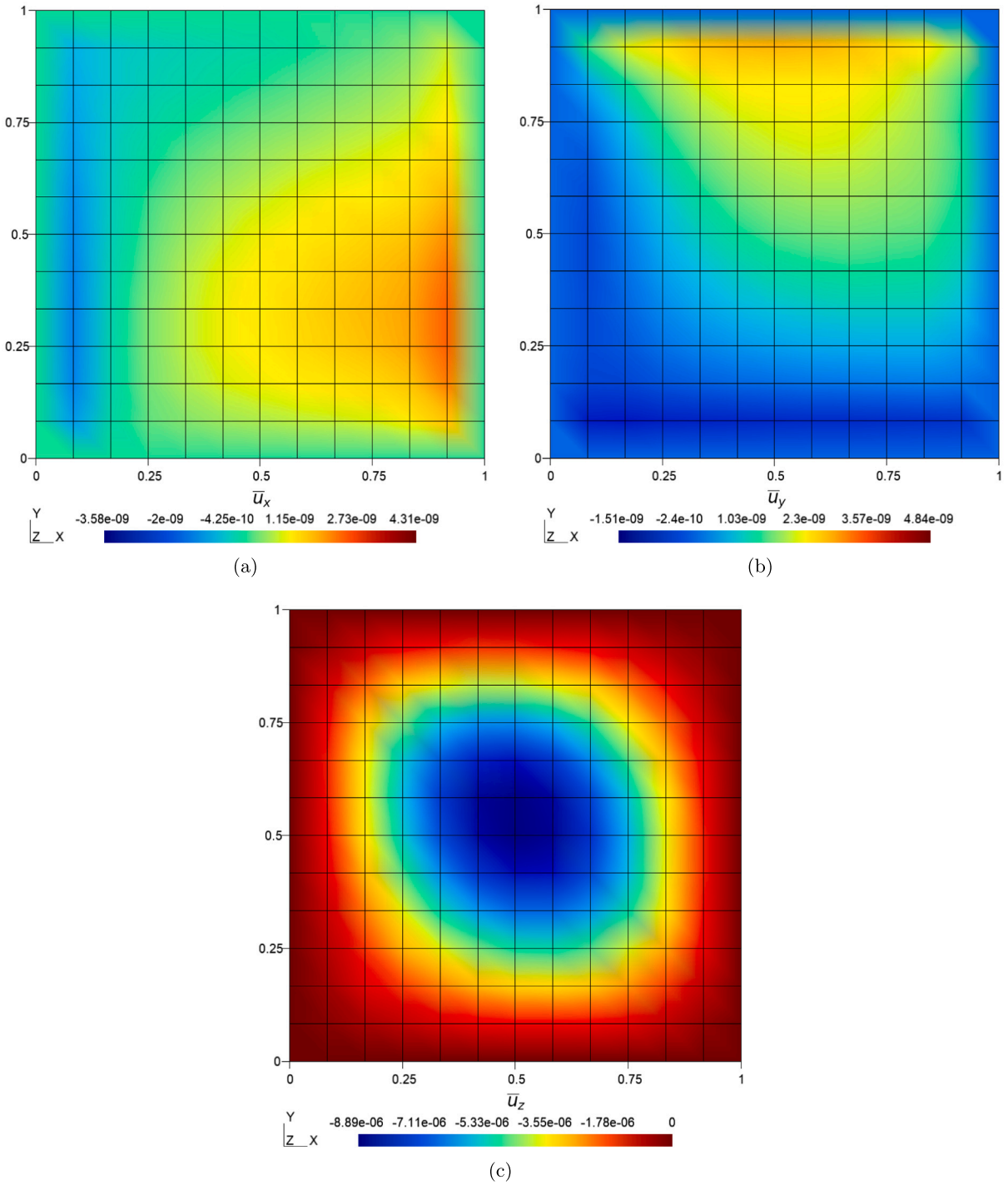

Fig. 6. Contour plots of the dimensionless displacements on plate middle plane ($z = 0$), 3LM4, case 1, $a/h = 10$.

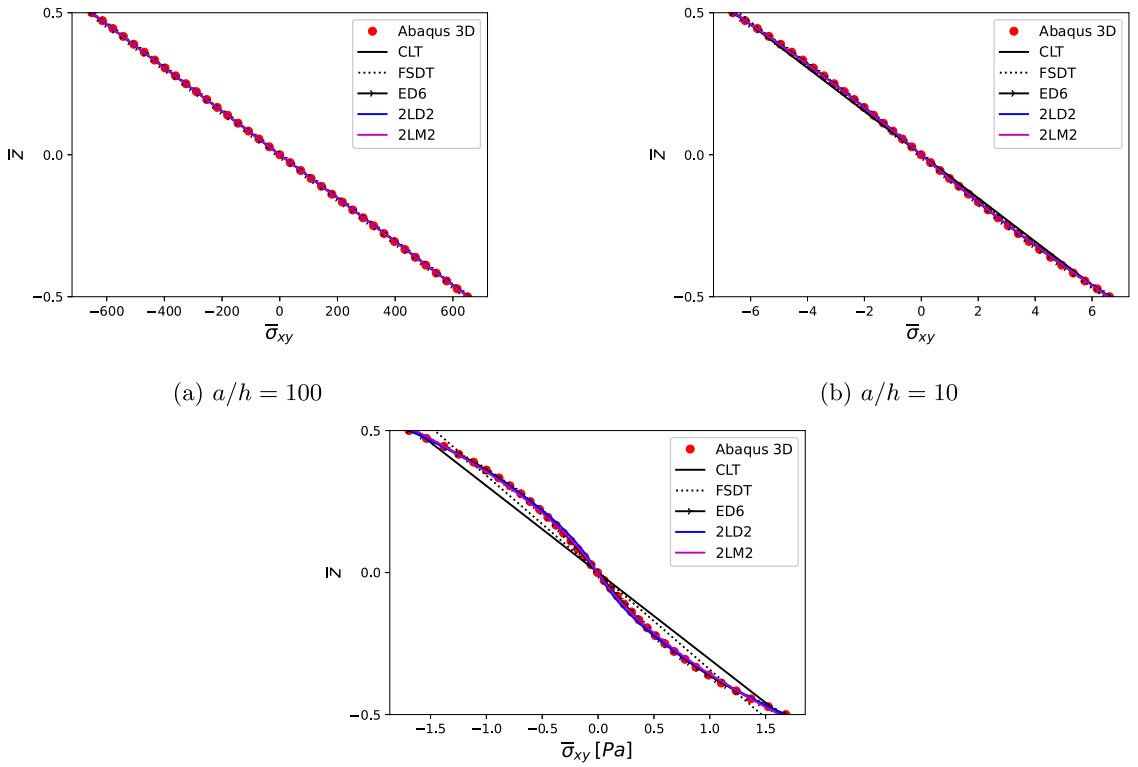

(a) $a/h = 100$

(b) $a/h = 10$

(c) $a/h = 5$

Fig. 7. Dimensionless in-plane normal stress $\bar{\sigma}_{xy}$ at $(a/2, b/2)$ versus the dimensionless thickness, case 1.

The generic unknown component $f = f(x, y, z)$ can be approximated as:

$$f(x, y, z) = F_\tau(z)\, g_\tau(x, y) \ , \quad \tau = 0,\ 1,\ \ldots,\ N \ , \tag{14}$$

where f is a displacement component in a formulation derived by the PVD, whereas it can also be an out-of-plane stress component when a RMVT formulation is considered. F_τ is an approximation function along the thickness and g_τ is an unknown two-dimensional function accounting for the in-plane variation. According to Einstein's notation, a twice repeated index implies a sum over that index range. Finally, N is the approximation order. Both N and F_τ can be imposed a-priori. This feature of CUF allows to obtain multiple theories in the same formulation.

According to the choice of F_τ, it is possible to obtain ESL or LW models. In the ESL case, the number of unknowns does not depend on the number of layers of the structure. For this reason, the total stiffness contributes are obtained as a weighted average of the layers stiffness along the thickness. Taylor's polynomials are the most common choice to develop an ESL model:

$$F_\tau(z) = z^\tau \ , \quad \tau = 0,\ 1,\ \ldots,\ N \ . \tag{15}$$

ESL models are able to predict the general response of relatively thin laminates and are characterized by a reduced computational cost. On the other hand, they are not able to predict accurately the behavior of thick plates especially in the case of a high degree of anisotropy. Since they are based on C^∞ approximation functions, ESL approaches cannot describe correctly the zigzag displacements effect (nonetheless, it could be possible to include this feature by adding Murakami's function, as explained in Carrera [49]).

In order to improve the accuracy of the model, it is possible to consider a LW approach, where the kinematics of each layer is formulated independently. In this case, the number of unknowns depends on the number of layers, and it is necessary to impose the continuity of the problem main unknowns at an interface between consecutive layers. LW models usually use Lagrange or Legendre polynomials to approximate the unknown fields. In the LW approach, the approximation along the thickness direction reads:

$$f^k(x, y, z) = F_b(z)\, g_b^k(x, y) + F_r(z)\, g_r^k(x, y) + F_t(z)\, g_t^k(x, y) \ , \quad r = 2,\ \ldots,\ N \ , \tag{16}$$

where the superscript 'k' refers to a specific layer of the structure with k ranging between 1 and N_l, the latter being the total number of layers. Subscripts 't' and 'b' refer to the top and the bottom faces of the generic layer, respectively. In the case of Legendre polynomials, the through the thickness approximating functions are:

$$\begin{aligned} &F_t\left(z(\xi_k)\right) = \frac{P_0 + P_1}{2}, \quad F_b\left(z(\xi_k)\right) = \frac{P_0 - P_1}{2}, \\ &F_r\left(z(\xi_k)\right) = P_r - P_{r-2}, \quad r = 2,\ \ldots,\ N \ , \end{aligned} \tag{17}$$

where $P_i = P_i(\xi_k)$ is the i-order Legendre polynomial defined in the domain of the kth layer and $-1 < \xi_k < 1$. LW models are able to predict the zigzag through-the-thickness behavior of the displacement field. Nevertheless, LW models demand a higher computational cost, since they provide an independent approximation for every layer of the plate.

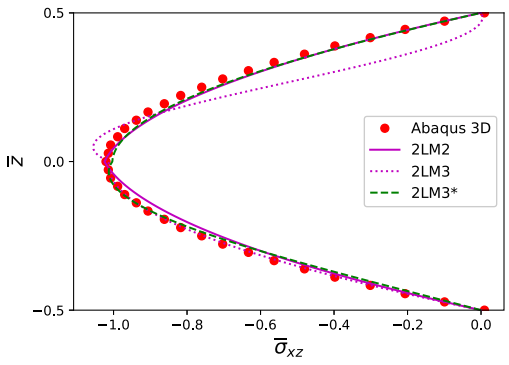

(a) $a/h = 100$

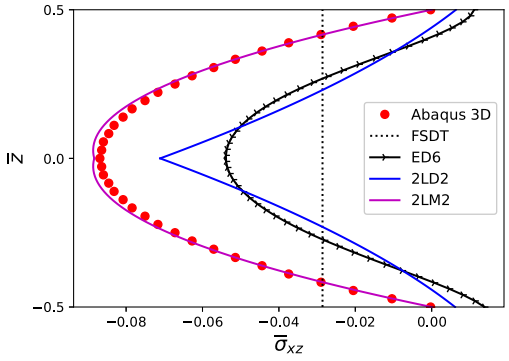

(b) $a/h = 10$

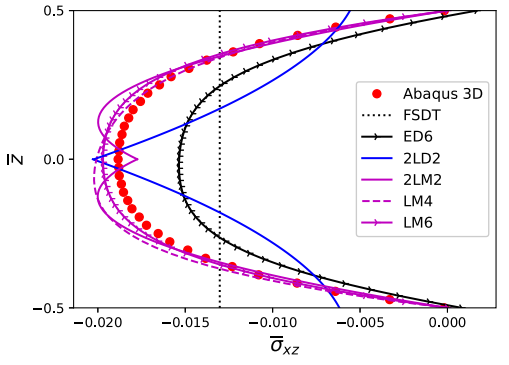

(c) $a/h = 5$

Fig. 8. Dimensionless out-of-plane shear stress $\bar{\sigma}_{xz}$ at $(a/2, b/2)$ versus the dimensionless thickness, case 1.

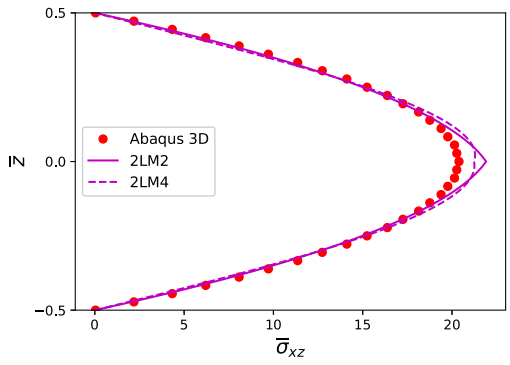

(a) $a/h = 100$

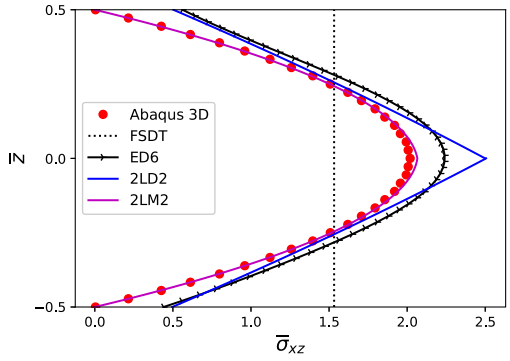

(b) $a/h = 10$

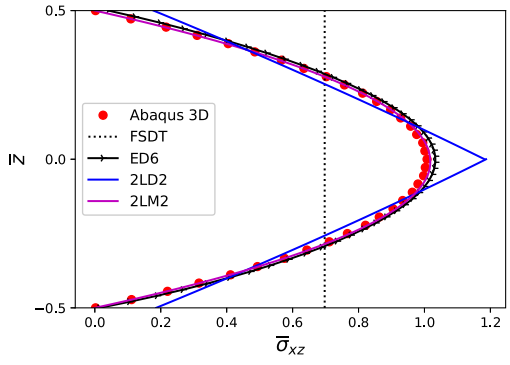

(c) $a/h = 5$

Fig. 9. Dimensionless out-of-plane shear stress $\bar{\sigma}_{xz}$ at $(a/4, b/2)$ versus the dimensionless thickness, case 1.

When a FEM approximation is applied, the shape functions need to be introduced into the formulation. In the case of a bi-dimensional model, Eq. (14) becomes:

$$f(x, y, z) = F_\tau(z)\, N_i(x, y)\, g_{\tau i}\,, \quad \tau = 0,\ 1,\ \ldots,\ N, \quad i = 1,\ \ldots,\ N_n\,, \tag{18}$$

where N_i represents the shape functions that are used for the approximation of the unknowns into the plane of the plate and N_n is equal to the number of nodes used for the domain discretization. Classical Lagrange shape functions are used. They are not here presented for the sake of brevity but they can be found in [50].

2.4. Acronym system

An acronym system is introduced in order to identify the derived theories. This system is shown in Fig. 3. The first letter refers to the approximation level that is used: 'E' corresponds to ESL models, while 'L' corresponds to LW models. The second letter refers to the variational statement: 'D' or 'M' stand for PVD or RMVT, respectively. The last number refers to the expansion order used along the plate thickness. The first number, when present, refers to the number of virtual layers that have been used for the LW model to represent every single physical layer: if the number at the beginning of the acronym is not present, it

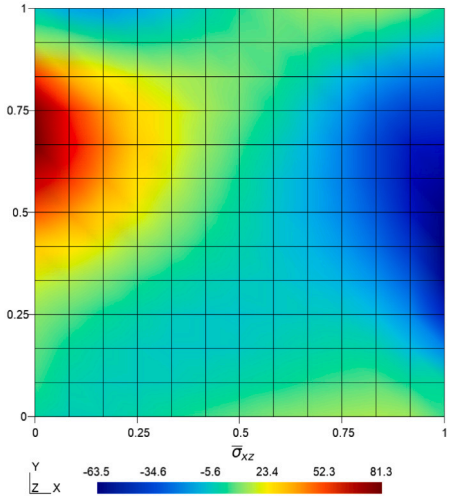

(a) 2LM3*, $a/h = 100$

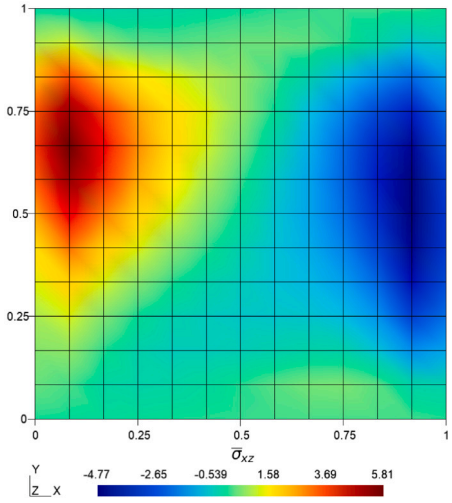

(b) 2LM2, $a/h = 10$

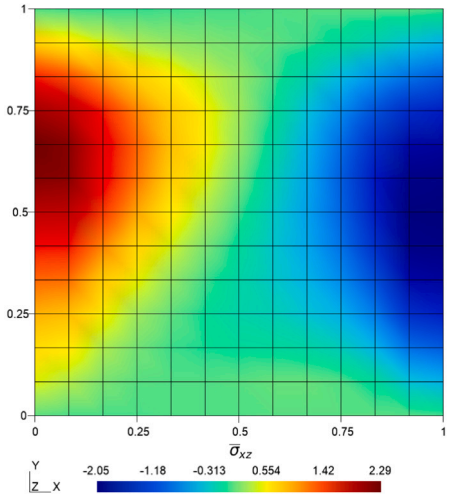

(c) LM6, $a/h = 5$

Fig. 10. Contour plots of the dimensionless transverse stress $\bar{\sigma}_{xz}$ on plate middle plane ($z = 0$), case 1.

is tacitly assumed that only one virtual layer has been used for each physical layer.

For example, in EDN models, the displacement field can be expressed in the following form:

$$\begin{aligned} u_x &= u_{x0} + u_{x1} z + u_{x2} z^2 + \ \cdots + u_{xN} z^N \ , \\ u_y &= u_{y0} + u_{y1} z + u_{y2} z^2 + \ \cdots + u_{yN} z^N \ , \\ u_z &= u_{z0} + u_{z1} z + u_{z2} z^2 + \ \cdots + u_{zN} z^N . \end{aligned} \tag{19}$$

In a vectorial form:

$$\mathbf{u} = F_0 \mathbf{u}_0 + F_1 \mathbf{u}_1 + \ \cdots + F_N \mathbf{u}_N = F_\tau \mathbf{u}_\tau \ , \quad \tau = 0, \ 1, \ \ldots, \ N \ , \tag{20}$$

being $F_\tau = z^\tau$ and $\mathbf{u}_\tau = \mathbf{u}_\tau (x, y)$. Also, classical theories are obtained as a particular case of the ED1 solution: Classical Lamination Theory and First-order Shear Deformation Theory are indicated as CLT and FSDT, respectively. FSDT is obtained through the penalization of the u_{z1} term, while for CLT also transverse shear stresses need to be penalized. The material stiffness matrix is reduced to account for a plane stress state in both CLT and FSDT.

In LW theories, N refers to the approximation order used in every layer. For LDN solutions, only displacements are considered as unknowns:

$$\mathbf{u}^k = F_0 \mathbf{u}_0^k + F_1 \mathbf{u}_1^k + \cdots + F_N \mathbf{u}_N^k = F_\tau \mathbf{u}_\tau^k \ , \quad \tau = 0, \ 1 \ \ldots, \ N \ , \quad k = 1, \ 2, \ \ldots, \ N_l \ . \tag{21}$$

For LMN solutions, also transverse stresses are included among the unknowns. Indeed, the transverse stresses field can be expressed as:

$$\boldsymbol{\sigma}_n^k = F_b \boldsymbol{\sigma}_b^k + F_r \boldsymbol{\sigma}_r^k + F_t \boldsymbol{\sigma}_t^k \ , \quad r = 2, \ \ldots, \ N \ , \quad k = 1, \ 2, \ \ldots, \ N_l \ . \tag{22}$$

It can be observed that ESL theories can be considered as a particular case of LW ones. While in the first case the integration along the thickness is performed in order to represent composite properties through an equivalent single layer, for the second case the integration is computed layer by layer. This allows to represent the kinematic of each layer separately for LW models.

Unless otherwise stated, LDN solutions are obtained with Lagrange polynomials with equally spaced nodes, whereas LMN ones are obtained with Legendre polynomials. The symbol '$*$' refers to the case where Lagrange polynomials are used considering Chebyshev-Lobatto nodes. This kind of nodes distribution has been proven to improve the convergence of numerical solutions [51] and it can be expressed as:

$$\xi_i = -\cos\left(\frac{i \cdot \pi}{N}\right) \in [-1, 1] \ , \ i = 0, \ \ldots, N . \tag{23}$$

2.5. Stiffness matrices expression

In the PVD case, the primary unknown field is the displacements field. Considering Eq. (18), the displacements field can be written as follows:

$$\mathbf{u} = F_\tau N_i \begin{Bmatrix} q_{x\tau i} \\ q_{y\tau i} \\ q_{z\tau i} \end{Bmatrix} = F_\tau N_i \mathbf{q}_{\tau i} \ . \tag{24}$$

Through the substitution of Eqs. (3), (6) and (24) into Eq. (9), the governing equations of the PVD method can be obtained:

$$\begin{aligned} &\int_\Omega \delta \boldsymbol{q}_{\tau i}^T \left[\mathbf{D}_p^T \left(N_i \mathbf{I}\right) \widetilde{\mathbf{Z}}_{pp}^{\tau s} \mathbf{D}_p \left(N_j \mathbf{I}\right) + \mathbf{D}_p^T \left(N_i \mathbf{I}\right) \widetilde{\mathbf{Z}}_{pn}^{\tau s} \mathbf{D}_{n\Omega} \left(N_j \mathbf{I}\right) \right. \\ &+ \mathbf{D}_p^T \left(N_i \mathbf{I}\right) \widetilde{\mathbf{Z}}_{pn}^{\tau s, z} \left(N_j \mathbf{I}\right) + \\ &+ \mathbf{D}_{n\Omega}^T \left(N_i \mathbf{I}\right) \widetilde{\mathbf{Z}}_{np}^{\tau s} \mathbf{D}_p \left(N_j \mathbf{I}\right) + \mathbf{D}_{n\Omega}^T \left(N_i \mathbf{I}\right) \widetilde{\mathbf{Z}}_{nn}^{\tau s} \mathbf{D}_{n\Omega} \left(N_j \mathbf{I}\right) \\ &+ \mathbf{D}_{n\Omega}^T \left(N_i \mathbf{I}\right) \widetilde{\mathbf{Z}}_{nn}^{\tau s, z} \left(N_j \mathbf{I}\right) + \\ &+ \left(N_i \mathbf{I}\right) \widetilde{\mathbf{Z}}_{np}^{\tau, z s} \mathbf{D}_p \left(N_j \mathbf{I}\right) + \left(N_i \mathbf{I}\right) \widetilde{\mathbf{Z}}_{nn}^{\tau, z s} \mathbf{D}_{n\Omega} \left(N_j \mathbf{I}\right) \\ &\left. + \left(N_i \mathbf{I}\right) \widetilde{\mathbf{Z}}_{nn}^{\tau, z s, z} \left(N_j \mathbf{I}\right) \right] \boldsymbol{q}_{sj} d\Omega = \delta L e \ , \end{aligned} \tag{25}$$

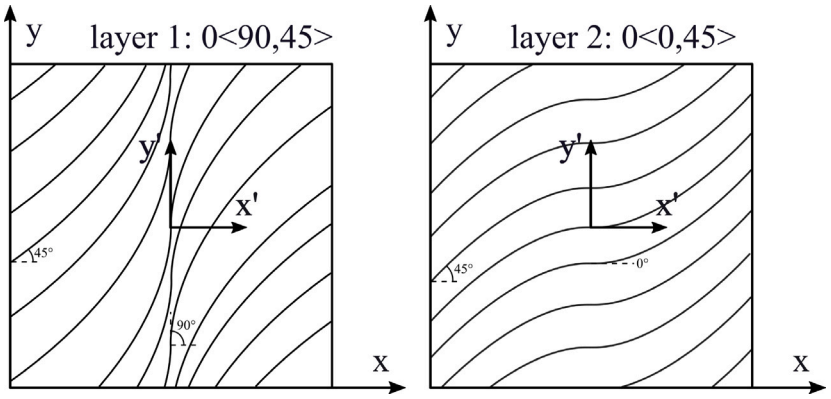

Fig. 11. In-plane fibers variation path and stacking sequence, cases 2 and 3.

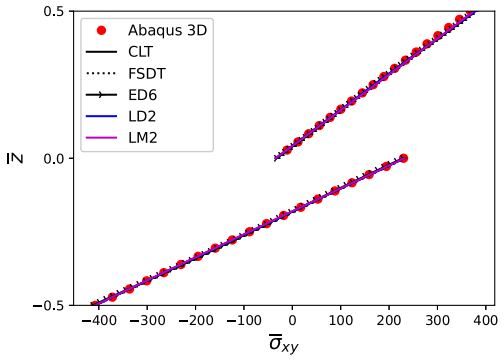

(a) $a/h = 100$

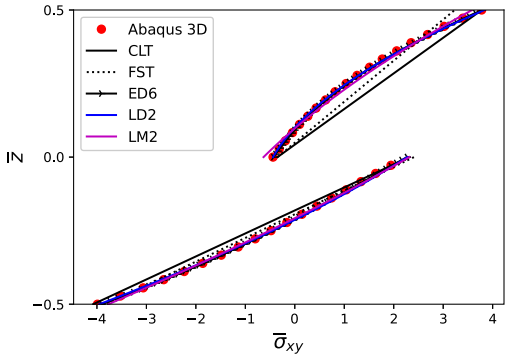

(b) $a/h = 10$

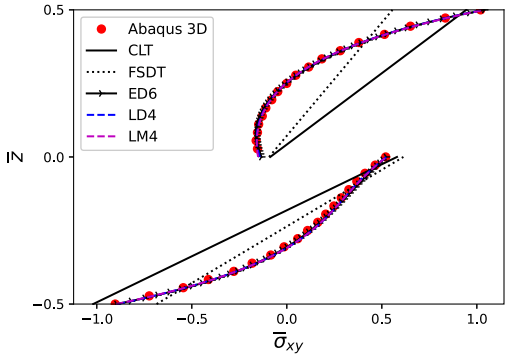

(c) $a/h = 5$

Fig. 12. Dimensionless in-plane shear stress $\bar{\sigma}_{xy}$ at $(a/4, b/2)$ versus the dimensionless thickness, case 2.

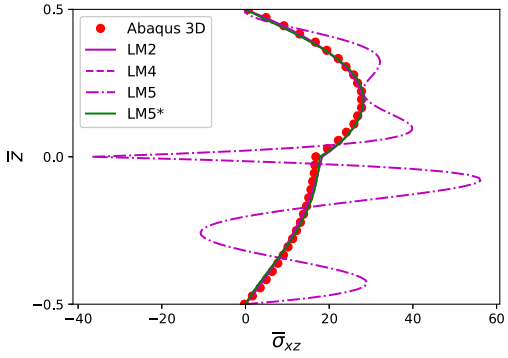

(a) $a/h = 100$

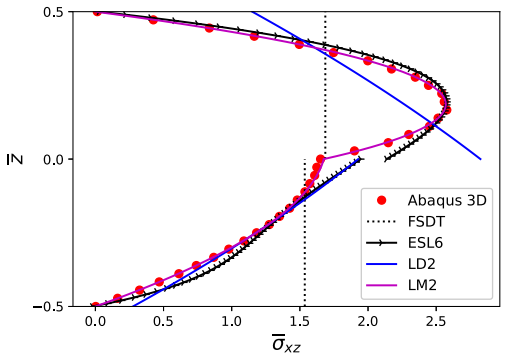

(b) $a/h = 10$

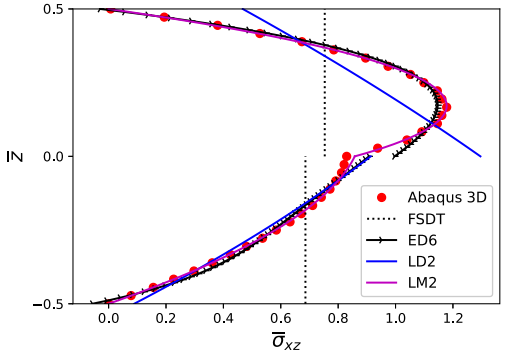

(c) $a/h = 5$

Fig. 13. Dimensionless transverse shear stress $\bar{\sigma}_{xz}$ at $(a/4, b/2)$ versus the dimensionless thickness, case 2.

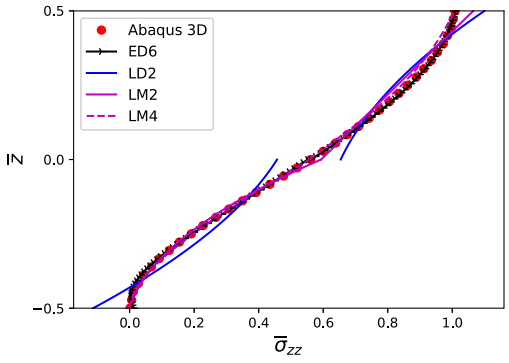

Fig. 14. Dimensionless transverse normal stress $\bar{\sigma}_{zz}$ at $(a/4, b/2)$ versus the dimensionless thickness, case 2, $a/h = 5$.

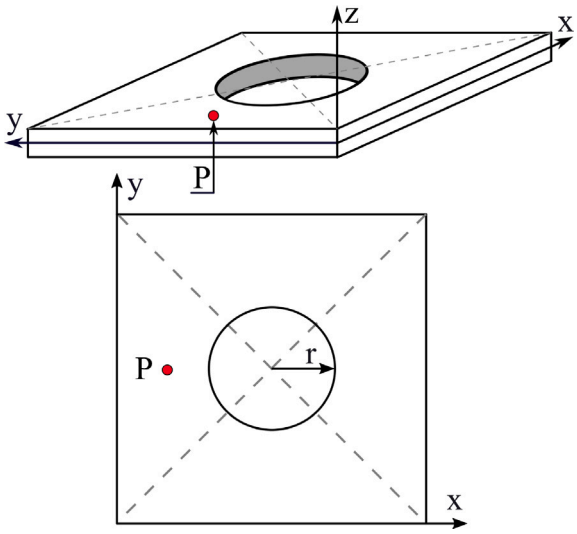

Fig. 15. Geometry of case 3: the red dot represents the point P where results have been plotted.

where:

$$\left(\widetilde{\mathbf{Z}}^{\tau s}_{wr}, \widetilde{\mathbf{Z}}^{\tau_{z} s}_{wr}, \widetilde{\mathbf{Z}}^{\tau s_{z}}_{wr}, \widetilde{\mathbf{Z}}^{\tau_{z} s_{z}}_{wr}\right) = \left(\widetilde{\mathbf{C}}_{wr} E_{\tau s}, \widetilde{\mathbf{C}}_{wr} E_{\tau_{z} s}, \widetilde{\mathbf{C}}_{wr} E_{\tau s_{z}}, \widetilde{\mathbf{C}}_{wr} E_{\tau_{z} s_{z}}\right) : \quad w, r = p, n \,, \tag{26}$$

$$\left(E_{\tau s}, E_{\tau_{z} s}, E_{\tau s_{z}}, E_{\tau_{z} s_{z}}\right) = \int_{h} \left(F_{\tau} F_{s}, F_{\tau_{z}} F_{s}, F_{\tau} F_{s_{z}}, F_{\tau_{z}} F_{s_{z}}\right) dz. \tag{27}$$

Index 'z' when preceded by a comma refers to the derivative in the thickness direction. In a compact vectorial form, Eq. (25) reads:

$$\delta \boldsymbol{q}^{T}_{\tau i} \mathbf{K}^{\tau s i j} \boldsymbol{q}_{s j} = \delta \boldsymbol{q}^{T}_{\tau i} \boldsymbol{P}_{\tau i} \,, \tag{28}$$

where $\mathbf{K}^{\tau s i j}$ is a 3x3 Fundamental Nucleus (FN). $\mathbf{P}^{\tau i}$ is the FN of the external loads vector. Through the loops on the indices τ, s, i and j it is possible to build the stiffness matrix and the loads vector of the whole plate element.

In the RMVT case, also transverse stresses represent an unknown field:

$$\boldsymbol{\sigma}_{n} = F_{\tau} N_{i} \begin{Bmatrix} g_{xz\tau i} \\ g_{yz\tau i} \\ g_{zz\tau i} \end{Bmatrix} = F_{\tau} N_{i} \mathbf{g}_{\tau i} \,. \tag{29}$$

Through the substitution of Eq. (3), (11), (24) and (29) into Eq. (10), the governing equations of the RMVT can be obtained:

$$\begin{aligned} &\int_{\Omega} \delta \boldsymbol{q}^{T}_{\tau i} \left[\mathbf{D}^{T}_{p}\left(N_{i}\mathbf{I}\right) \hat{\mathbf{Z}}^{\tau s}_{pp} \mathbf{D}_{p}\left(N_{j}\mathbf{I}\right)\right] \boldsymbol{q}_{s j} + \delta \boldsymbol{q}^{T}_{\tau i} \left[\, \mathbf{D}^{T}_{p}\left(N_{i}\mathbf{I}\right) \hat{\mathbf{Z}}^{\tau s}_{pn}\left(N_{j}\mathbf{I}\right)\right. \\ &+ \mathbf{D}^{T}_{n\Omega}\left(N_{i}\mathbf{I}\right)\left(E_{\tau s}\mathbf{I}\right)\left(N_{j}\mathbf{I}\right) + \\ &+ \left(N_{i}\mathbf{I}\right)\left(E_{\tau_{z} s}\mathbf{I}\right)\left(N_{j}\mathbf{I}\right)\left.\right] \boldsymbol{g}_{s j} + \delta \boldsymbol{g}^{T}_{\tau i} \left[\, \left(N_{i}\mathbf{I}\right)\left(E_{\tau s}\mathbf{I}\right)\mathbf{D}_{n\Omega}\left(N_{j}\mathbf{I}\right)\right. \\ &+ \left(N_{i}\mathbf{I}\right)\left(E_{\tau s_{z}}\mathbf{I}\right)\left(N_{j}\mathbf{I}\right) + \\ &- \left(N_{i}\mathbf{I}\right) \hat{\mathbf{Z}}^{\tau s}_{np} \mathbf{D}_{p}\left(N_{j}\mathbf{I}\right)\left.\right] \boldsymbol{q}_{s j} - \delta \boldsymbol{g}^{T}_{\tau i}\left(N_{i}\mathbf{I}\right) \hat{\mathbf{Z}}^{\tau s}_{nn}\left(N_{j}\mathbf{I}\right) \boldsymbol{g}_{s j} d\Omega = \delta L_{e} \,, \end{aligned} \tag{30}$$

where:

$$\left(\hat{\mathbf{Z}}^{\tau s}_{wr}, \hat{\mathbf{Z}}^{\tau_{z} s}_{wr}, \hat{\mathbf{Z}}^{\tau s_{z}}_{wr}, \hat{\mathbf{Z}}^{\tau_{z} s_{z}}_{wr}\right) = \left(\hat{\mathbf{C}}_{wr} E_{\tau s}, \hat{\mathbf{C}}_{wr} E_{\tau_{z} s}, \hat{\mathbf{C}}_{wr} E_{\tau s_{z}}, \hat{\mathbf{C}}_{wr} E_{\tau_{z} s_{z}}\right) : \quad w, r = p, n. \tag{31}$$

In a compact form:

$$\begin{aligned} &\delta \boldsymbol{q}^{T}_{\tau i} \mathbf{K}^{\tau s i j}_{uu} \boldsymbol{q}_{s j} + \delta \boldsymbol{q}^{T}_{\tau i} \mathbf{K}^{\tau s i j}_{u\sigma} \boldsymbol{g}_{s j} = \delta \boldsymbol{q}^{T}_{\tau i} \boldsymbol{P}_{\tau i} \,, \\ &\delta \boldsymbol{g}^{T}_{\tau i} \mathbf{K}^{\tau s i j}_{\sigma u} \boldsymbol{q}_{s j} + \delta \boldsymbol{g}^{T}_{\tau i} \mathbf{K}^{\tau s i j}_{\sigma\sigma} \boldsymbol{g}_{s j} = 0. \end{aligned} \tag{32}$$

In this case, four fundamental nuclei are obtained. The in-plane integrals are computed through Gauss quadrature so it is important to consider a correct number of Gauss points in order to obtain correct results. Since the material stiffness coefficients are not constant, it will be necessary to increase the number of Gauss points according to the variational law of fibers angle. Reduced integration is used in order to correct the shear locking phenomenon. A grid of 4×4 Gauss points is used for the fully integrated terms, while a 2×2 grid is used for the reduced ones.

3. Numerical results and discussion

Three benchmark problems are considered in this section: a monolayer plate, a multilayer plate and a multilayer plate with a central circular cut out. For each case, a square plate ($a = b = 1$ m) is considered. Parametric studies are performed considering different aspect ratios ($a/h = 100, 10, 5$). In all cases, the plates are clamped at the four edges and a constant pressure $p_z = 10$ kPa is applied on the top ($z = h/2$). Material properties are represented in Table 1. Reference solutions are represented by Abaqus 3D models where quadratic solid elements with reduced integration and three degrees of freedom per node (C3D20R) are used. Since the Abaqus 3D solutions consider a constant fibers orientation within each element, a refined in-plane mesh is needed in order to obtain accurate results. For CUF solutions, nine-node square elements are used (QUAD9). For each case study, a preliminary convergence analysis is carried out to identify the appropriate mesh for CUF and Abaqus solutions. Results are normalized as follows:

$$\bar{u}_{i} = \frac{u_{i}}{a} \text{ with } i = x, y, z \,, \tag{33}$$

$$\bar{\sigma}_{i,j} = \frac{\sigma_{i,j}}{p_{z}} \text{ with } i, j = x, y, z \,, \tag{34}$$

where $\bar{z} = z/h$. Percentage errors are evaluated as follows:

$$\delta = \frac{|v_{CUF} - v_{Abaqus3D}|}{|v_{Abaqus3D}|} \cdot 100 \text{ with } v = \bar{u}_{i}, \bar{\sigma}_{i,j} \,, \; i, j = x, y, z. \tag{35}$$

3.1. Monolayer plate

The first case corresponds to a monolayer plate. It is assumed that fibers angle is function of y'. For this problem axes x' and y' of local reference system of the fibers path are coincident with axes x and y of the global reference system of the plate. Therefore the characteristic length of Eq. (8) is set to $d = b$. Angle variational law is expressed as $90 < 0, 90 >$ and it is represented in Fig. 4. This law is taken from Viglietti et al. [32], where it is applied on a rectangular

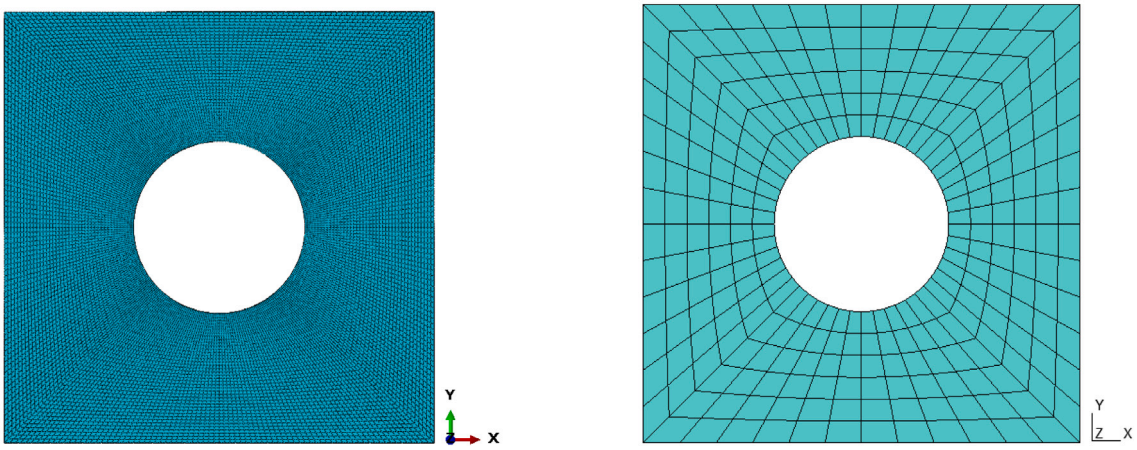

(a) Abaqus 3D. (b) CUF.

Fig. 16. Representation of the mesh used for case 3, $a/h = 10, 5$.

Table 1
Material properties.

	E_1	$E_2 = E_3$	G_{12}	G_{13}	G_{23}	ν_{12}	ν_{13}	ν_{23}
Case 1	50 GPa	10 GPa	5 GPa	5 GPa	5 GPa	0.25	0.25	0.25
Cases 2, 3	137.9 GPa	8.96 GPa	7.1 GPa	7.1 GPa	6.21 GPa	0.3	0.3	0.49

Table 2
Number of degrees of freedom, case 1.

	DOF
Abaqus 3D	4,457,151
3LM4	48,750
2LM2	18,750
3LD4	24,375
2LD2	9,375
ED6	13,125
ED2	5,625
FSDT	3,750
CLT	3,750

Table 3
Dimensionless transverse displacement $\bar{u}_z \cdot -10^6$ at $(a/2, b/2, h/2)$, case 1.

a/h	100	10	5
Abaqus 3D	6544	8.768	1.877
3LM4	6527	8.760	1.875
2LM2	6530	8.781	1.890
3LD4	6526	8.759	1.876
2LD2	6526	8.725	1.858
ED6	6526	8.757	1.875
ED2	6522	8.435	1.741
FSDT	6542	8.481	1.712
CLT	6521	6.521	0.815

plate for vibration analyses. Abaqus reference solution contains 140 elements along each side and 18 elements along the thickness. Results are plotted along the thickness in correspondence of plate central point $(a/2, b/2)$. For CUF results, a 12 × 12 mesh is considered. The number of Degrees Of Freedom (DOF) associated to every model are represented in Table 2. It is possible to observe that high-order CUF models are characterized by a number of DOF which is two magnitude orders smaller than the Abaqus reference solution. This indicates a great advantage in terms of computational cost. It is worth noting that FSDT and CLT have the same number of DOF because of the way they have been implemented within CUF. Indeed, even if for the CLT an artificial shear stiffness in introduced to lock the rotational degree of freedom, the linear system to be solved in both cases has the same dimension. The table shows that LM models have double DOF number in comparison with LD ones, considering the same expansion order and the same amount of virtual layers. In this way it is possible to compare different theories, considering the computational cost of each model in terms of degrees of freedom. Table 3 shows the transverse normal displacement at plate center top $(a/2, b/2, h/2)$, considering several values of the ratio a/h. For thicker plates, classical theories and low order displacement based theories show higher variations with respect to the reference solution. LMN* solutions are not reported since they show the same results of the correspondent LMN ones. Figs. 5 show the dimensionless displacements along $\bar{z}$ for $a/h = 10$. $\bar{u}_x$ and $\bar{u}_y$ components are accurately approximated by the FSDT classical model, for this reason no higher-order theories are reported in Figs. 5a and 5b. In these two figures, the CLT model shows lower accuracy and it reaches an $\bar{u}_x$ error of 16.60% at $\bar{z} = -0.5$. In Fig. 5[num=c]5(c), the 3LM4 model is the closest one to the Abaqus reference solution, with an $\bar{u}_z$ maximum error of 0.33%. CLT and FSDT models are not reported in the $\bar{u}_z$ plot, since they are too far from the other theories. For example, the maximum errors of CLT is 25.92%. Figs. 6 show the distribution of the dimensionless displacement field, obtained with the 3LM4 model, at plate middle plane $(z = 0)$ for $a/h = 10$. It is possible to observe that, in all the figures, the plots are not symmetrical, because of the fibers angle variation along y' axis. In Fig. 6a, $\bar{u}_x$ is negative on the left side of the plate $(x = 0)$ and becomes positive on the right

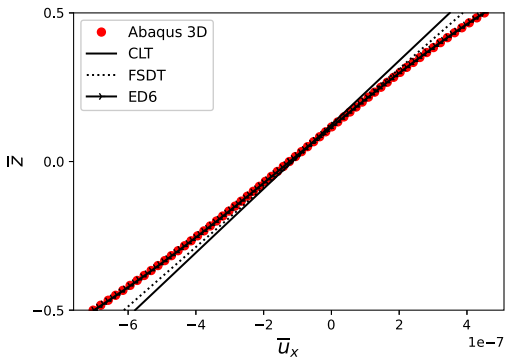

(a)

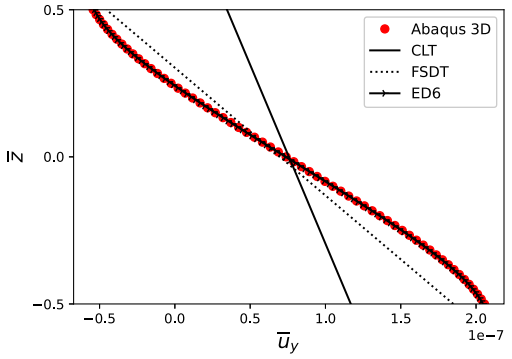

(b)

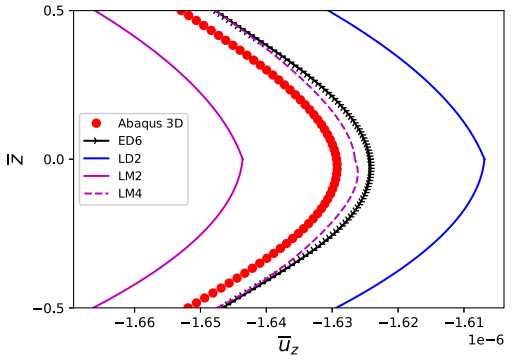

(c)

Fig. 17. Dimensionless displacements at point P versus the dimensionless thickness, case 3, $a/h = 10$.

side ($x = a$). Conversely, in Fig. 6b, the $\bar{u}_y$ distribution follows the variation of fibers orientation along y' axis. $\bar{u}_y$ is negative where fibers are perpendicular to x' ($\theta = 90°$) and becomes mostly positive where fibers are perpendicular to y' ($\theta = 180°$). In Fig. 6c, the $\bar{u}_z$ distribution is slightly shifted towards the upper part of the plate at $y = b$. Indeed, the plate has a stiffer behavior where the fibers are perpendicular to the clamped boundaries ($y = 0$).

Figs. 7 show the in-plane shear stress $\bar{\sigma}_{xy}$ at plate center for different plate side-to-thickness ratios. For thin plates, all theories show a good approximation of the reference solution. When a/h is decreased, higher-order theories continue to match the reference solution, while classical ones give a progressively worse estimation. Similar considerations can

Table 4
Dimensionless in-plane normal stress $-1 \times \bar{\sigma}_{xx}$ at $(a/4, b/2, h/2)$, case 2.

a/h	100	10	5
Abaqus 3D	967.580	12.020	4.253
LM4*	987.394	12.163	4.331
LM4	987.500	12.163	4.331
LM2*	983.937	11.587	3.818
LM2	983.911	11.587	3.818
LD4	1008.792	12.291	4.336
LD2	998.481	12.232	4.293
ED6	994.297	12.222	4.340
ED2	986.167	10.817	3.321
FSDT	992.994	9.941	2.565
CLT	992.820	9.924	2.480

be done for the other in-plane stress components, which are not presented for sake of brevity. Figs. 8 show the transverse shear stress $\bar{\sigma}_{xz}$ at plate center considering three different side-to-thickness ratio values (100, 10 and 5). Displacement based theories do not approximate the transverse shear stresses well, even if multiple virtual layers are applied in the case of a layer-wise approach. Only higher-order mixed models model match the Abaqus solution. In Fig. 8a, the 2LM3 model shows convergence problems due to the Runge phenomenon that are overcome by applying Lagrange polynomials with Chebyshev-Lobatto nodes, as demonstrated by the 2LM3* solution. It is important to consider that by decreasing the plate thickness, the transverse stresses become more and more negligible with respect to in-plane ones. For example, it is possible to notice that for $a/h = 100$, the maximum value of $\bar{\sigma}_{xx}$ is almost three orders of magnitude higher than the maximum value of $\bar{\sigma}_{xz}$. In Fig. 8b, higher-order LM theories are not shown since they give an approximation which is close to the 2LM2 model. In Fig. 8c, the results which use Chebyshev-Lobatto nodes are not presented since no convergence problems have been detected even for high-orders. LW theories show a discontinuity of the first derivative in correspondence of the interface between virtual layers. Indeed, while ESL models assume a C^∞ function for describing primary variables along the thickness, LW ones do not assure the continuity of function derivatives along $\bar{z}$. Displacement-based theories are not represented in Fig. 8a, since they are too far from the reference solution. The dimensionless transverse shear stress $\bar{\sigma}_{xz}$ has also been plotted at $(a/4, b/2)$ in Figs. 9 for comparison purposes. Indeed, at $(a/4, b/2)$, $\bar{\sigma}_{xz}$ values are one order of magnitude bigger than the ones computed at $(a/2, b/2)$. Fig. 9a shows that in this case when $a/h = 100$, the 2LM2 model shows an error of 7.44% at $\bar{z} = 0$. This error can be reduced to 4.12% by upgrading the model to the fourth order. Fig. 9b and Fig. 9c show that for $a/h = 10$, 5 the 2LM2 model is sufficient for a good approximation of $\bar{\sigma}_{xz}$. In these cases also the ED6 model shows good results since a single layer is considered and the anisotropy of the plate is limited. Finally, Figs. 10 show the distribution of the dimensionless out-of-plane stress $\bar{\sigma}_{xz}$, at plate middle plane ($z = 0$) for $a/h = 100$, 10, 5. The shape of the plots is similar for each a/h value, since $\bar{\sigma}_{xz}$ has a positive value in proximity of $x = 0$ and becomes negative at $x = a$. It is possible to observe that the positive and negative regions of $\bar{\sigma}_{xz}$ become bigger from Fig. 10a to Fig. 10c, when the side-to-thickness ratio a/h is decreased.

3.2. Multilayer plate

Case 2 is taken from Demasi et al. [40] and corresponds to a multilayer plate. The plate is composed of two layers with the same thickness ($h/2$). It is assumed that fibers angle is function of x' only. For this problem, axes x' and y' of the local reference system of the fibers path are aligned with axes x and y of the global reference system of the plate, but their origin is placed on the center of the

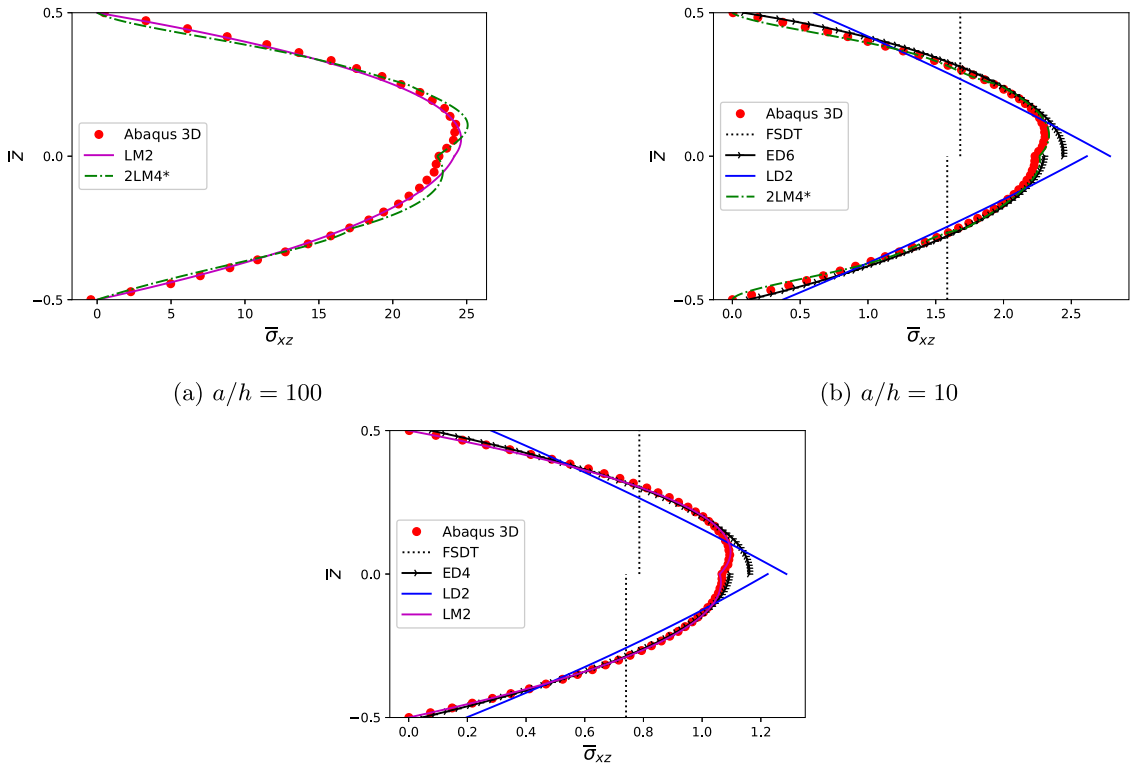

(a) $a/h = 100$ (b) $a/h = 10$

(c) $a/h = 5$

Fig. 18. Dimensionless transverse shear stress $\bar{\sigma}_{xz}$ at point P versus the dimensionless thickness, case 3.

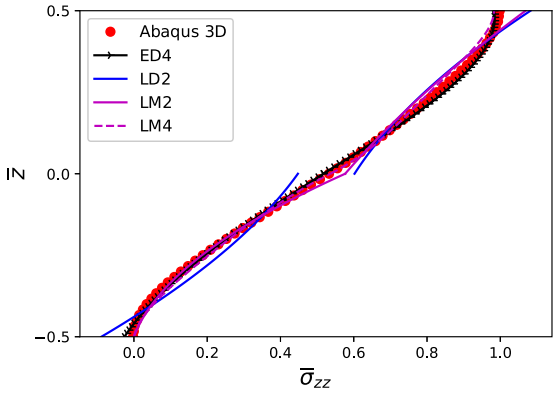

Fig. 19. Dimensionless transverse normal stress $\bar{\sigma}_{zz}$ at point P versus the dimensionless thickness, case 3, $a/h = 5$.

plate $(a/2, b/2)$. In this case, $a/2$ is considered as characteristic length in Eq. (8) ($d = a/2$). fibers angle behavior is represented for both layers, starting from the bottom, as: $0 < 90, 45 >$ for layer 1 and $0 < 0, 45 >$ for layer 2. The stacking sequence is represented in Fig. 11. As for the previous case, the Abaqus reference solution contains 140 elements along each side and 18 elements along the thickness. Results are plotted along the dimensionless thickness coordinate at $(a/4, b/2)$. For CUF results, a 16×16 mesh is considered. Table 4 shows the value of the dimensionless in-plane normal stress $\bar{\sigma}_{xx}$ at plate top for different theories and side-to-thickness ratios. For thin plates, in-plane stresses become predominant with respect to out-of-plane ones and classical theories get closer to the reference solution. For this case, the plots of the dimensionless displacements are not presented since they are similar to the ones of the previous case and similar considerations can be done. In Figs. 12, the variation of $\bar{\sigma}_{xy}$ versus $\bar{z}$ is presented for $a/h = 100$, 10 and 5, respectively. In this case the loss of linearity due to the thickness increasing is more evident in comparison with the previous case. This phenomenon causes the classical theories to fail in the prediction of the in-plane shear stress, while higher-order theories continue to match the reference solution. It is also possible to notice a discontinuity at the interface between the two layers due to the mechanical properties' discontinuity. Figs. 13 show the dimensionless transverse stress $\bar{\sigma}_{xz}$ along the thickness. In this case, only mixed theories are able to match the reference solution. For $a/h = 10$ and 5, the LM2 model is sufficient to give a valid approximation, for this reason higher-order approximations are not shown. For $a/h = 100$, $\bar{\sigma}_{xz}$ is characterized by an error of 8.97% at the interface between the layers. This error can be reduced to 6.58% and 5.78% with the LM4 and LM5* models, respectively. In this case the convergence issue due to the Runge phenomenon of mixed high-order models is more evident. The comparison of LM5 and LM5* solutions shows how the results can be improved thanks to the Chebyshev-Lobatto nodes distribution. Displacement based theories are not represented in Fig. 13a because of their excessive distance from the reference solution. Transverse stresses have to fulfill equilibrium between layers interfaces and satisfy the load boundary conditions at plates top and bottom. This means that $\bar{\sigma}_{xz}$, $\bar{\sigma}_{yz}$ and $\bar{\sigma}_{zz}$ should be continuous at the interface between layers and should have the same value of external loads at plate top and bottom. Since only a constant pressure load aligned with z axis is applied, $\bar{\sigma}_{xz}$ and $\bar{\sigma}_{yz}$ have to be equal to zero at $z = h/2$ and $z = -h/2$. The dimensionless transverse normal stress $\bar{\sigma}_{zz}$ for $a/h = 5$ is represented in Fig. 14. This stress should be zero at $z = -h/2$ and equal to the external load at $z = h/2$. Those conditions are not satisfied by LD theories, since, in those cases, stresses are computed during the post processing through Hooke's law by using displacements derivatives and their continuity is not assured at the interface between virtual layers.

Table 5
Dimensionless in-plane normal stress $-1 \times \bar{\sigma}_{xx}$ at point P for $z = h/2$, case 3.

a/h	100	10	5
Abaqus 3D	621.031	4.164	0.297
LM4*	590.555	4.079	0.313
LM4	602.890	4.096	0.307
LM2*	609.466	4.652	0.828
LM2	609.121	4.655	0.830
LD4	580.100	3.814	0.218
LD2	593.907	3.872	0.378
ED4	592.177	3.898	0.255
ED2	607.555	5.426	0.990
FSDT	556.488	5.524	1.398
CLT	563.920	5.630	1.404

The ED6 model shows a good approximation of $\bar{\sigma}_{zz}$ because of the high-order polynomial that is used to predict $\bar{u}_z$ along the thickness without virtual interfaces. For RMVT theories, transverse stresses are considered together with displacements as primary variables: this allows to fulfill the equilibrium conditions a priori. Inter-layer equilibrium is imposed during the assembly of the global stiffness matrix, while stress top and bottom boundary conditions are imposed as boundary conditions of the transverse stresses.

3.3. Multilayer plate with a central hole

In this last analysis, the plates present a central circular hole. The material properties and the stacking sequence are the same of the second case. The center of the cut out is placed at $(a/2, b/2)$ and its radius is $r = 0.2$ m. In this case, the Abaqus reference solution is made of 384000 elements for $a/h = 10$ and 5; 12800 elements are defined into the plane of the plate and 30 elements are defined along the thickness. When $a/h = 100$, in order to avoid stress gradient problems related to the high elements' aspect ratio, the number of elements into the plane is increased to 20 000 and the number of elements along the thickness is reduced to 18. Results are plotted along thickness at point P, shown in Fig. 15, whose coordinates are: $x_P = (a/2 - r)/2, y_P = b/2$. For CUF results, 288 plate elements have been used. Figs. 16 show the mesh used for this analysis case when $a/h = 10, 5$. Table 5 shows the values of $\bar{\sigma}_{xx}$ at plate top for different values of the side-to-thickness ratio. The comparison with Table 4 shows that for $a/h = 100$ and 5, these values are higher for the plate with the central cut out. Dimensionless displacements are plotted in Figs. 17 along $\bar{z}$ for $a/h = 10$. In comparison with case 1, in this case CLT and FSDT models are not sufficient to guarantee a correct approximation of the in-plane components $\bar{u}_x$ and $\bar{u}_y$ because of the more complex geometry. For this reason, in Figs. 17a and 17b, the errors of CLT at $\bar{z} = -0.5$ are 17.58% and 43.17%, respectively. In Fig. 17c, it is possible to observe that the LM4 model is the closest to the reference solution (maximum error of 0.32%), followed by the ED6 one (maximum error of 0.34%). The dimensionless in-plane stresses plots are not reported in this case since they show the same behavior of the previous cases. Figs. 18 present the plots of the dimensionless transverse shear stress $\bar{\sigma}_{xz}$ versus the dimensionless thickness at point P for $a/h = 100$, 10 and 5. In Fig. 18a, the percentage error of the LM2 solution at $\bar{z} = 0$ is 4.48% and it can be reduced to 0.53% with the 2LM4* model. For very thick plates ($a/h = 5$), both mixed and high-order ESL models are able to predict the normal transverse stress as observed in Fig. 19.

4. Conclusions

A general numerical framework for deriving several plate finite elements models for the analysis of VAT structures is presented in this paper. The main outcome of this work is represented by the development of RMVT CUF plate finite elements for the study of 2D VAT plates. The possibility to choose the expansion order a priori through CUF allows to develop a wide family of bi-dimensional models. This is useful to predict the static response of VAT plates, which appear to be a promising alternative to classical straight fibers composites. Although the formulation is general, linear laws have been considered to describe fibers path and it has been assumed that the direction along which fibers angle can change corresponds to one of the main in-plane directions of the global problem reference system (x or y). Three cases have been analyzed to consider different laminations and geometries. Abaqus 3D reference solutions have been used for the validation of the proposed models. ESL and LW theories have been both considered for PVD theories, while only LW approach has been developed for RMVT models. The results lead to the following conclusions:

- All models show good displacements approximation. This is mostly observable for transverse displacement u_z.
- CLT and FSDT models show a good approximation of displacements and in-plane stresses for thin plates. On the other hand, they are based on classical hypotheses which do not allow to correctly predict transverse stresses. This represents a strong limitation, especially for failure analyses, where transverse stresses represent an important factor.
- ESL models allow to represent the displacement field through a continuous function, with continuous derivative, along the thickness. This can be a problem when zigzag displacement field occurs, as in the case of layered plates. Despite this, ESL models are still useful because of their reduced computational cost.
- LW models allow to describe the kinematic of each layer separately from the others layers. Usually, this corresponds to more accurate results but higher computational cost.
- RMVT models allow to fulfill compatibility and equilibrium conditions of transverse stresses a priori. For thin plates, high-order RMVT models show convergence problems, which can be solved by using Lagrange polynomials with the Chebyshev-Lobatto nodes distribution.
- Higher-order displacement based theories show good results for displacements and in-plane stresses. Usually, those theories do not correctly predict transverse stresses.
- Mixed theories are usually more accurate than displacements ones, especially for transverse stresses. Conversely, they require a higher computational cost. Hence, employing LW mixed models proves beneficial when a more accurate depiction of through-thickness behavior is required, particularly in cases where transverse stresses play an important role and need to be predicted accurately. Whereas LW and ESL displacement-based models show a satisfying prediction of in-plane displacement and stresses. Finally, classical theories like FSDT and CLT, are more appropriate for thin plates, since a linear behavior is considered for in-plane displacements and stresses.

In conclusion, the application of RMVT within CUF to VAT plates for static analyses has shown great promise in improving the accuracy and efficiency of modeling these complex structures. However, the potential of this approach is not limited to static analyses alone. Potential prospects foresee the use of this framework for dynamic, buckling and failure analyses of VATs.

CRediT authorship contribution statement

D.A. Iannotta: Methodology, Software, Validation, Formal analysis, Writing – original draft, Writing – review & editing. **G. Giunta:** Conceptualization, Methodology, Writing – review & editing, Supervision, Project administration, Funding acquisition. **M. Montemurro:** Conceptualization, Methodology, Writing – review & editing, Supervision, Project administration, Funding acquisition.

Declaration of competing interest

The authors declare the following financial interests/personal relationships which may be considered as potential competing interests: Gaetano Giunta, Domenico Andrea Iannotta reports financial support was provided by Luxembourg National Research Fund. Marco Montemurro reports financial support was provided by French National Research Agency.

Data availability

Data will be made available on request.

Acknowledgments

This research was funded in part by the Luxembourg National Research Fund (FNR), grant reference INTER/ANR/21/16215936 GLAMOUR-VSC. For the purpose of open access, and in fulfillment of the obligations arising from the grant agreement, the author has applied a Creative Commons Attribution 4.0 International (CC BY 4.0) license to any Author Accepted Manuscript version arising from this submission. M. Montemurro is grateful to French National Research Agency for supporting this work through the research project GLAMOUR-VSC (Global-LocAl two-level Multi-scale optimization strategy accOUnting for pRocess-induced singularities to design Variable Stiffness Composites) ANR-21-CE10-0014.

Appendix. Expression of the fundamental nuclei

This appendix reports the FN of the structure stiffness matrix for the PVD and RMVT variational statements. The components of the FN for the PVD case can be written as follows in the case of an orthotropic material:

$$
\begin{aligned}
K_{xx}^{\tau sij} &= \int_{\Omega} \left(\widetilde{Z}_{pp11}^{\tau s} N_{j,x} N_{i,x} + \widetilde{Z}_{pp16}^{\tau s} N_{j,y} N_{i,x} + \widetilde{Z}_{pp16}^{\tau s} N_{j,x} N_{i,y} \right. \\
&\quad \left. + \widetilde{Z}_{pp66}^{\tau s} N_{j,y} N_{i,y} + \widetilde{Z}_{nn44}^{\tau_z s_z} N_j N_i \right) d\Omega \,, \\
K_{xy}^{\tau sij} &= \int_{\Omega} \left(\widetilde{Z}_{pp12}^{\tau s} N_{j,y} N_{i,x} + \widetilde{Z}_{pp16}^{\tau s} N_{j,x} N_{i,x} + \widetilde{Z}_{pp26}^{\tau s} N_{j,y} N_{i,y} \right. \\
&\quad \left. + \widetilde{Z}_{pp66}^{\tau s} N_{j,x} N_{i,y} + \widetilde{Z}_{nn45}^{\tau_z s_z} N_j N_i \right) d\Omega \,, \\
K_{xz}^{\tau sij} &= \int_{\Omega} \left(\widetilde{Z}_{pn13}^{\tau s_z} N_j N_{i,x} + \widetilde{Z}_{pn36}^{\tau s_z} N_j N_{i,y} + \widetilde{Z}_{nn44}^{\tau_z s} N_{j,x} N_i + \widetilde{Z}_{nn45}^{\tau_z s} N_{j,y} N_i \right) d\Omega \,, \\
K_{yx}^{\tau sij} &= \int_{\Omega} \left(\widetilde{Z}_{pp12}^{\tau s} N_{j,x} N_{i,y} + \widetilde{Z}_{pp26}^{\tau s} N_{j,y} N_{i,y} + \widetilde{Z}_{pp16}^{\tau s} N_{j,x} N_{i,x} \right. \\
&\quad \left. + \widetilde{Z}_{pp66}^{\tau s} N_{j,y} N_{i,x} + \widetilde{Z}_{nn45}^{\tau_z s_z} N_j N_i \right) d\Omega \,, \\
K_{yy}^{\tau sij} &= \int_{\Omega} \left(\widetilde{Z}_{pp22}^{\tau s} N_{j,y} N_{i,y} + \widetilde{Z}_{pp26}^{\tau s} N_{j,x} N_{i,y} + \widetilde{Z}_{pp26}^{\tau s} N_{j,y} N_{i,x} \right. \\
&\quad \left. + \widetilde{Z}_{pp66}^{\tau s} N_{j,x} N_{i,x} + \widetilde{Z}_{nn55}^{\tau_z s_z} N_j N_i \right) d\Omega \,, \\
K_{yz}^{\tau sij} &= \int_{\Omega} \left(\widetilde{Z}_{pn23}^{\tau s_z} N_j N_{i,y} + \widetilde{Z}_{pn36}^{\tau s_z} N_j N_{i,x} + \widetilde{Z}_{nn45}^{\tau_z s} N_{j,x} N_i + \widetilde{Z}_{nn55}^{\tau_z s} N_{j,y} N_i \right) d\Omega \,, \\
K_{zx}^{\tau sij} &= \int_{\Omega} \left(\widetilde{Z}_{nn44}^{\tau s_z} N_j N_{i,x} + \widetilde{Z}_{nn45}^{\tau s_z} N_j N_{i,y} + \widetilde{Z}_{np13}^{\tau_z s} N_{j,x} N_i + \widetilde{Z}_{np36}^{\tau_z s} N_{j,y} N_i \right) d\Omega \,, \\
K_{zy}^{\tau sij} &= \int_{\Omega} \left(\widetilde{Z}_{nn45}^{\tau s_z} N_j N_{i,x} + \widetilde{Z}_{nn55}^{\tau s_z} N_j N_{i,y} + \widetilde{Z}_{np23}^{\tau_z s} N_{j,y} N_i + \widetilde{Z}_{np36}^{\tau_z s} N_{j,x} N_i \right) d\Omega \,, \\
K_{zz}^{\tau sij} &= \int_{\Omega} \left(\widetilde{Z}_{nn44}^{\tau s} N_{j,x} N_{i,x} + \widetilde{Z}_{nn45}^{\tau s} N_{j,y} N_{i,x} + \widetilde{Z}_{nn45}^{\tau s} N_{j,x} N_{i,y} \right. \\
&\quad \left. + \widetilde{Z}_{nn55}^{\tau s} N_{j,y} N_{i,y} + \widetilde{Z}_{nn33}^{\tau_z s_z} N_j N_i \right) d\Omega .
\end{aligned}
\tag{36}
$$

The subscripts 'x' and 'y' when preceded by a comma refer to the derivative versus the corresponding in-plane direction. The components of the FN for the RMVT case can be written as follows:

$$
\begin{aligned}
K_{uux}^{\tau sij} &= \int_{\Omega} \left(\hat{Z}_{pp11}^{\tau s} N_{j,x} N_{i,x} + \hat{Z}_{pp31}^{\tau s} N_{j,x} N_{i,y} + \hat{Z}_{pp13}^{\tau s} N_{j,y} N_{i,x} + \hat{Z}_{pp33}^{\tau s} N_{j,y} N_{i,y} \right) d\Omega \,, \\
K_{uuxy}^{\tau sij} &= \int_{\Omega} \left(\hat{Z}_{pp12}^{\tau s} N_{j,y} N_{i,x} + \hat{Z}_{pp32}^{\tau s} N_{j,y} N_{i,y} + \hat{Z}_{pp13}^{\tau s} N_{j,x} N_{i,x} + \hat{Z}_{pp33}^{\tau s} N_{j,x} N_{i,y} \right) d\Omega \,, \\
K_{uuyx}^{\tau sij} &= \int_{\Omega} \left(\hat{Z}_{pp21}^{\tau s} N_{j,x} N_{i,y} + \hat{Z}_{pp31}^{\tau s} N_{j,x} N_{i,x} + \hat{Z}_{pp23}^{\tau s} N_{j,y} N_{i,y} + \hat{Z}_{pp33}^{\tau s} N_{j,y} N_{i,x} \right) d\Omega \,, \\
K_{uuyy}^{\tau sij} &= \int_{\Omega} \left(\hat{Z}_{pp22}^{\tau s} N_{j,y} N_{i,y} + \hat{Z}_{pp32}^{\tau s} N_{j,y} N_{i,x} + \hat{Z}_{pp23}^{\tau s} N_{j,x} N_{i,y} + \hat{Z}_{pp33}^{\tau s} N_{j,x} N_{i,x} \right) d\Omega \,, \\
K_{uuxz}^{\tau sij} &= 0 \,, \quad K_{uuyz}^{\tau sij} = 0 \,, \quad K_{uuzx}^{\tau sij} = 0 \,, \quad K_{uuzy}^{\tau sij} = 0 \,, \quad K_{uuzz}^{\tau sij} = 0 \,, \\
K_{u\sigma xx}^{\tau sij} &= \int_{\Omega} \left(E_{\tau,z^s} N_j N_i \right) d\Omega \,, \quad K_{u\sigma xz}^{\tau sij} = \int_{\Omega} \left(\hat{Z}_{pn13}^{\tau s} N_j N_{i,x} + \hat{Z}_{pn33}^{\tau s} N_j N_{i,y} \right) d\Omega \,, \\
K_{u\sigma yy}^{\tau sij} &= \int_{\Omega} \left(E_{\tau,z^s} N_j N_i \right) d\Omega \,, \quad K_{u\sigma yz}^{\tau sij} = \int_{\Omega} \left(\hat{Z}_{pn23}^{\tau s} N_j N_{i,y} + \hat{Z}_{pn33}^{\tau s} N_j N_{i,x} \right) d\Omega \,, \\
K_{u\sigma zx}^{\tau sij} &= \int_{\Omega} \left(E_{\tau s} N_j N_{i,x} \right) d\Omega \,, \quad K_{u\sigma zy}^{\tau sij} = \int_{\Omega} \left(E_{\tau s} N_j N_{i,y} \right) d\Omega \,, \\
K_{u\sigma zz}^{\tau sij} &= \int_{\Omega} \left(E_{\tau,z^s} N_j N_i \right) d\Omega \,, \\
K_{u\sigma xy}^{\tau sij} &= 0 \,, \quad K_{u\sigma yx}^{\tau sij} = 0 \,, \\
K_{\sigma uxx}^{\tau sij} &= \int_{\Omega} \left(E_{\tau s,z} N_j N_i \right) d\Omega \,, \quad K_{\sigma uxz}^{\tau sij} = \int_{\Omega} \left(E_{\tau s} N_{j,x} N_i \right) d\Omega \,, \\
K_{\sigma uyy}^{\tau sij} &= \int_{\Omega} \left(E_{\tau s,z} N_j N_i \right) d\Omega \,, \\
K_{\sigma uyz}^{\tau sij} &= \int_{\Omega} \left(E_{\tau s} N_{j,y} N_i \right) d\Omega \,, \quad K_{\sigma uzx}^{\tau sij} = -\int_{\Omega} \left(\hat{Z}_{np31}^{\tau s} N_{j,x} N_i - \hat{Z}_{np33}^{\tau s} N_{j,y} N_i \right) d\Omega \,, \\
K_{\sigma uzy}^{\tau sij} &= -\int_{\Omega} \left(\hat{Z}_{np32}^{\tau s} N_{j,y} N_i - \hat{Z}_{np33}^{\tau s} N_{j,x} N_i \right) d\Omega \,, \\
K_{\sigma uzz}^{\tau sij} &= \int_{\Omega} \left(E_{\tau s,z} N_j N_i \right) d\Omega \,, \\
K_{\sigma uxy}^{\tau sij} &= 0 \,, \quad K_{\sigma uyx}^{\tau sij} = 0 \,, \\
K_{\sigma\sigma xx}^{\tau sij} &= -\int_{\Omega} \left(\hat{Z}_{nn11}^{\tau s} N_j N_i \right) d\Omega \,, \quad K_{\sigma\sigma xy}^{\tau sij} = -\int_{\Omega} \left(\hat{Z}_{nn12}^{\tau s} N_j N_i \right) d\Omega \,, \\
K_{\sigma\sigma yx}^{\tau sij} &= -\int_{\Omega} \left(\hat{Z}_{nn21}^{\tau s} N_j N_i \right) d\Omega \,, \quad K_{\sigma\sigma xx}^{\tau sij} = -\int_{\Omega} \left(\hat{Z}_{nn22}^{\tau s} N_j N_i \right) d\Omega \,, \\
K_{\sigma\sigma xz}^{\tau sij} &= 0 \,, \quad K_{\sigma\sigma yz}^{\tau sij} = 0 \,, \quad K_{\sigma\sigma zx}^{\tau sij} = 0 \,, \quad K_{\sigma\sigma zy}^{\tau sij} = 0 \,, \quad K_{\sigma\sigma zz}^{\tau sij} = 0.
\end{aligned}
\tag{37}
$$

References

[1] Sikora A, Gaff M, Sethy AK, Fantuzzi N, Horáček P. Bending work of laminated materials based on densified wood and reinforcing components. Compos Struct 2021;274:114319.
[2] Ghiasi H, Fayazbakhsh K, Pasini D, Lessard L. Optimum stacking sequence design of composite materials Part II: Variable stiffness design. Compos Struct 2010;93(1):1–13.
[3] Hyer MW, Charette RF. Innovative design of composite structures: The use of curvilinear fiber format in composite structure design. Technical report, 1990.
[4] Hyer MW, Lee HH. Innovative design of composite structures: the use of curvilinear fiber format to improve buckling resistance of composite plates with central circular holes. Technical report, 1990.
[5] Luo JH, Gea HC. Optimal orientation of orthotropic materials using an energy based method. Struct Optim 1998;15:230–6.
[6] Gürdal Z, Olmedo R. In-plane response of laminates with spatially varying fiber orientations-variable stiffness concept. AIAA J 1993;31(4):751–8.
[7] Gürdal Z, Tatting BF, Wu CK. Variable stiffness composite panels: Effects of stiffness variation on the in-plane and buckling response. Composites A 2008;39(5):911–22.
[8] Gupta A, Pradyumna S. Geometrically nonlinear bending analysis of variable stiffness composite laminated shell panels with a higher-order theory. Compos Struct 2021;276:114527.
[9] Akhavan Hamed, Ribeiro Pedro, Moura MFSF De. Large deflection and stresses in variable stiffness composite laminates with curvilinear fibres. Int J Mech Sci 2013;73:14–26.
[10] Günay M Gökhan, Timarci Taner. Static analysis of thin-walled laminated composite closed-section beams with variable stiffness. Compos Struct 2017;182:67–78.
[11] Sharma Narayan, Swain Prasant Kumar, Maiti Dipak Kumar, Singh Bhrigu Nath. Static and free vibration analyses and dynamic control of smart variable stiffness laminated composite plate with delamination. Compos Struct 2022;280:114793.
[12] Groh RMJ, Weaver PM. A computationally efficient 2D model for inherently equilibrated 3D stress predictions in heterogeneous laminated plates, Part I: Model formulation. Compos Struct 2016;156:171–85.

[13] Groh RMJ, Weaver PM. A computationally efficient 2D model for inherently equilibrated 3D stress predictions in heterogeneous laminated plates, Part II: Model validation. Compos Struct 2016;156:186–217.
[14] Trinh LC, Ojo SO, Groh RMJ, Weaver PM. A mixed inverse differential quadrature method for static analysis of constant-and variable-stiffness laminated beams based on hellinger-reissner mixed variational formulation. Int J Solids Struct 2021;210:66–87.
[15] Sciascia G, Oliveri V, Weaver PM. Eigenfrequencies of prestressed variable stiffness composite shells. Compos Struct 2021;270:114019.
[16] Oliveri V, Milazzo A. A Rayleigh–Ritz approach for postbuckling analysis of variable angle tow composite stiffened panels. Comput Struct 2018;196:263–76.
[17] Montemurro M. An extension of the polar method to the first-order shear deformation theory of laminates. Compos Struct 2015;127:328–39.
[18] Montemurro M. The polar analysis of the third-order shear deformation theory of laminates. Compos Struct 2015;131:775–89.
[19] Montemurro M, Catapano A. On the effective integration of manufacturability constraints within the multi-scale methodology for designing variable angle-tow laminates. Compos Struct 2017;161:145–59.
[20] Catapano A, Montemurro M, Balcou J-A, Panettieri E. Rapid prototyping of variable angle-tow composites. Aerotecnica Missili & Spazio 2019;98(4):257–71.
[21] Montemurro M, Catapano A. A general b-spline surfaces theoretical framework for optimisation of variable angle-tow laminates. Compos Struct 2019;209:561–78.
[22] Fiordilino GA, Izzi MI, Montemurro M. A general isogeometric polar approach for the optimisation of variable stiffness composites: Application to eigenvalue buckling problems. Mech Mater 2021;153:103574.
[23] Catapano A, Montemurro M. Strength optimisation of variable angle-tow composites through a laminate-level failure criterion. J Optim Theory Appl 2020;187(3):683–706.
[24] Izzi MI, Catapano A, Montemurro M. Strength and mass optimisation of variable-stiffness composites in the polar parameters space. Struct Multidiscip Optim 2021;64(4):2045–73.
[25] Carrera E. Theories and finite elements for multilayered, anisotropic, composite plates and shells. Arch Comput Methods Eng 2002;9(2):87–140.
[26] Carrera E. Theories and finite elements for multilayered plates and shells: A unified compact formulation with numerical assessment and benchmarking. Arch Comput Methods Eng 2003;10(3):215–96.
[27] Carrera E, Giunta G, Brischetto S. Hierarchical closed form solutions for plates bent by localized transverse loadings. J Zhejiang Univ-Sci A 2007;8:1026–37.
[28] Carrera E, Giunta G. Hierarchical models for failure analysis of plates bent by distributed and localized transverse loadings. J Zhejiang Univ-Sci A 2008;9:600–13.
[29] Giunta G, Catapano A, Belouettar S. Failure indentation analysis of composite sandwich plates via hierarchical models. J Sandwich Struct Mater 2013;15(1):45–70.
[30] Hui Y, Xu R, Giunta G, De Pietro G, Hu H, Belouettar S, et al. Multiscale CUF-FE2 nonlinear analysis of composite beam structures. Comput Struct 2019;221:28–43.
[31] Hui Y, Bai X, Yang Y, Yang J, Huang Q, Liu X, et al. A data-driven CUF-based beam model based on the tree-search algorithm. Compos Struct 2022;300:116123.
[32] Viglietti A, Zappino E, Carrera E. Analysis of variable angle tow composites structures using variable kinematic models. Composites B 2019;171:272–83.
[33] Fallahi N, Viglietti A, Carrera E, Pagani A, Zappino E. Effect of fiber orientation path on the buckling, free vibration, and static analyses of variable angle tow panels. Facta Univ. Ser: Mech Eng 2020;18(2):165–88.
[34] Fallahi N, Carrera E, Pagani A. Application of GA optimization in analysis of variable stiffness composites. Int J Mater Metall Eng 2021;15(2):65–70.
[35] Sánchez-Majano AR, Azzara R, Pagani A, Carrera E. Accurate stress analysis of variable angle tow shells by high-order equivalent-single-layer and layer-wise finite element models. Materials 2021;14(21):6486.
[36] Pagani A, Sanchez-Majano AR. Influence of fiber misalignments on buckling performance of variable stiffness composites using layerwise models and random fields. Mech Adv Mater Struct 2022;29(3):384–99.
[37] Pagani A, Sanchez-Majano AR. Stochastic stress analysis and failure onset of variable angle tow laminates affected by spatial fibre variations. Compos C: Open Access 2021;4:100091.
[38] Sanchez-Majano AR, Pagani A, Petrolo M, Zhang C. Buckling sensitivity of tow-steered plates subjected to multiscale defects by high-order finite elements and polynomial chaos expansion. Materials 2021;14(11):2706.
[39] Demasi L, Ashenafi Y, Cavallaro R, Santarpia E. Generalized unified formulation shell element for functionally graded variable-stiffness composite laminates and aeroelastic applications. Compos Struct 2015;131:501–15.
[40] Demasi L, Biagini G, Vannucci F, Santarpia E. Equivalent single layer, zig-zag, and layer wise theories for variable angle tow composites based on the generalized unified formulation. Compos Struct 2017;177:54–79.
[41] Demasi L, Giacomo B, Federico V, Santarpia E, Rauno C. Generalized unified formulation-based bending analysis of variable angle tow panels in the presence of hole. In: AIAA/ASCE/AHS/ASC structures, structural dynamics, and materials conference, vol. 2018, no. 0210049. p. 2018.
[42] Santarpia E, Demasi L. Computational architecture based on Murakami's zig-zag function for the geometrically nonlinear analysis of variable angle tow laminates. In: AIAA scitech 2020 forum, 1 PartF, no. January. 2020, p. 0449.
[43] Vescovini R, Dozio L. A variable-kinematic model for variable stiffness plates: Vibration and buckling analysis. Compos Struct 2016;142:15–26.
[44] Tornabene F, Fantuzzi N, Bacciocchi M. Higher-order structural theories for the static analysis of doubly-curved laminated composite panels reinforced by curvilinear fibers. Thin-Walled Struct 2016;102:222–45.
[45] Carrera E, Demasi L. Classical and advanced multilayered plate elements based upon pvd and RMVT, Part 1: derivation of finite element matrices. Int J Numer Methods Eng 2002;55(2):191–231.
[46] Carrera E, Demasi L. Classical and advanced multilayered plate elements based upon pvd and RMVT, part 2: numerical implementations. Int J Numer Methods Eng 2002;55(3):253–91.
[47] Giunta G, Iannotta DA, Montemurro M. A FEM free vibration analysis of variable stiffness composite plates through hierarchical modeling. Materials 2002;16(13):4643.
[48] Reddy JN. Mechanics of laminated composite plates and shells: theory and analysis. CRC Press; 2003.
[49] Carrera E. On the use of the Murakami's zig-zag function in the modeling of layered plates and shells. Comput Struct 2004;82(7–8):541–54.
[50] Bathe K-J. Finite element procedures. Klaus-Jurgen Bathe; 2006.
[51] Mathews JH, Fink KD, et al. Numerical methods using MATLAB, vol. 4. NJ: Pearson prentice hall Upper Saddle River; 2004.